Quantum sensing tools to characterize physical, chemical and biological processes with magnetic resonance

Analia Zwick, Gonzalo A. Álvarez

PII: S2666-4410(23)00021-3
DOI: https://doi.org/10.1016/j.jmro.2023.100113
Reference: JMRO 100113

To appear in: *Journal of Magnetic Resonance Open*

Received date : 16 November 2022
Revised date : 21 March 2023
Accepted date : 24 March 2023

Please cite this article as: A. Zwick and G.A. Álvarez, Quantum sensing tools to characterize physical, chemical and biological processes with magnetic resonance, *Journal of Magnetic Resonance Open* (2023), doi: https://doi.org/10.1016/j.jmro.2023.100113.

Quantum sensing tools to characterize physical, chemical and biological processes with magnetic resonance

Analia Zwick[1, 2, 3] and Gonzalo A. Álvarez[1, 2, 3, *]

[1] *Centro Atómico Bariloche, CONICET, CNEA, Bariloche, Argentina*
[2] *Instituto Balseiro, CNEA, Universidad Nacional de Cuyo, Bariloche, Argentina*
[3] *Instituto de Nanociencia y Nanotecnologia, CNEA, CONICET, Bariloche, Argentina*

Nuclear Magnetic Resonance (NMR) plays a central role in developing quantum information sciences and technologies. Key features such as its non-invasive nature and the ability to process information on nuclear spins by versatile quantum control designs with electromagnetic fields, have made NMR to become a powerful technique for sensing systems from atomic and molecular scales with spectroscopy to millimeters in imaging. This brief overview provides quantum sensing tools with which we are contributing from Latin America, by combining quantum dynamical control and estimation strategies with NMR methods to probe physical, chemical, and biological processes. It introduces the basic and key concepts on how controlled spin-sensors can monitor the correlation dynamics of their environment, and selectively and optimally infer its relevant parameters. Then these concepts are illustrated with state-of-the-art implementations for characterizing (i) biological tissue microstructure with diffusion weighting imaging, (ii) quantum information dynamics and scrambling in out-of-equilibrium systems with solid-state NMR quantum simulations, and (iii) molecular structures by selective estimation of spin-spin couplings and online learning control designs with experimental proposals. We expect these concepts will motivate the development of quantum dynamical control of spin sensors to monitor systems in a variety of fields, and in particular to exploit the non-invasive strength of NMR, e.g. in biomedical diagnosis.

I. INTRODUCTION

Nuclear Magnetic Resonance (NMR) has a central role paving the way to the development of quantum technologies. It was one of the first experimental means to control quantum systems to process information [1–10], and thus inspired the development of quantum control methods in a wide variety of systems, such as cold atoms [11–13], ion traps [14–16], Rydberg atoms [17, 18], polar molecules [18, 19], nuclear spins in liquids and solids [20–25], and nitrogen-vacancy centers (NVc) in diamonds [26–31]. Furthermore, it inspires prompting crucial questions regarding the unique benefits and distinctions that quantum information offers compared to classical information: what is the inherent quantum nature of information, and what aspects cannot be replicated by classical systems? [3, 4, 32–40].

In general, novel control methods have emerged to extend the lifetime of quantum states [22, 41–49], manipulate and transfer them to specific destinations [22, 49–56]. These have influenced numerous application areas starting with quantum computing and simulation [20, 25, 57–61], and reaching applications of biological, chemical or technological interest where quantum systems play the role of sensors [21, 23, 24, 27, 62–74].

These quantum technologies are already part of our reality and a critical step towards their deployment is finding their optimization and robustness to extend their application areas. NMR is a technique very well developed on dynamical control methods for sensing a wide variety of systems, and therefore has an important role to play on the development of novel quantum sensing tools [75–77]. The broad scope and versatility of the quantum control methods is the strength of NMR. This allowed to test the first quantum information processing algorithms [1, 2, 6, 78] and can be a testbed for answering fundamental questions about quantum mechanics with quantum simulations [20, 25, 79–86].

Quantum sensing and sensors are of particular interest for this overview, as they will serve in applications ranging from thermometry [73, 87–89] and magnetometry [90, 91] to medical imaging [24, 66, 70, 87, 92–94] with subnanometer resolutions [24, 64, 66, 70, 72, 74, 95–97]. The simplest quantum sensor, is a qubit which is the basic unit of quantum information [3, 49, 98]. In its analogy to the classical bit, the qubit, represents a system with two well-defined physical properties such as, for example, two energy levels or particles with spin $\frac{1}{2}$. Here the sensor is a quantum system used as a sensitive probe of its environment, e.g., for measuring electric or magnetic fields, temperature, or pressure.

Quantum sensing can be approached through various strategies, as discussed in Ref. [98]. One of the most commonly used strategies involves utilizing a quantum system or coherence to probe physical quantities at atomic and nanoscales. While these strategies might not necessarily offer an advantage over classical devices in terms of introducing more efficient information processing, they can allow probing spatial scales that are not accessible by classical means. In this overview, we will mainly focus

* Corresponding author: gonzalo.alvarez@conicet.gov.ar

on this scenario, as it is closer to applications for sensing physical, chemical, and biological processes. However, exploiting quantum information that cannot be reproduced by classical systems, such as entanglement, can potentially introduce more sensitive quantum sensing strategies for extracting and processing information [80, 89, 98–100]. Depending on the experimental setup, quantum sensors can be accessed and controlled individually or in an ensemble.

Individual quantum-sensors have been shown to detect magnetic fields produced by individual electrons or nuclei, enabling the determination of subnanometer-scale structures of individual molecules [101–105]. This revolutionary tool has the potential to transform the fields of chemistry and biology, opening up new possibilities for precision medicine. Yet, while promising the detection by individual quantum systems, most probably these techniques will remain invasive approaches.

NMR detected by induction coils at room temperature address an ensemble of qubits composed of some 10^{20} identical copies of a nuclear spin in proper molecules. The qubit-sensor state in these cases is defined by an statistical mixture, that in some situations can be processed to generate pseudo-pure states [1–4, 8–10, 79, 106]. In this scenario, for example, the hydrogen's nuclear spins of the water molecules composing about of 70% of our body, serve as sensors of their environment. One of the NMR strengths compared to other quantum technologies that allow single qubit-sensor addressing, is that the signal of such an ensemble of sensors can be detected noninvasively independently if there exist or not a quantum advantage for processing the information.

This NMR strength also imposes a great challenge, how to extract the relevant information about microscopic, nanometer, and atomic scales, stored on the quantum sensors within the ensemble. For example, extracting quantitative microstructure information of living tissue by noninvasive imaging is a key element for understanding disease mechanisms and allowing early-stage diagnosis of pathologies [107–113]. Exploiting the restricted molecular diffusion of water molecules within tissues that contain structured media, the effective resolution of Magnetic Resonance Imaging (MRI) can be boosted to extract tissue microstructure features within a pixel far exceeding the resolution of standard MRI techniques [24, 66, 70, 93, 94, 114–125]. The key here is the design of suitable dynamical quantum-control strategies to codify this information into the spins signal evolution. This thus shows the importance of developing quantum sensing methods to extract efficiently and reliably this huge microscopic information.

A. Decoherence, the fragility of quantum systems

The main tool, and at the same time the main problem of this developing area, is that quantum sensors, like all quantum systems, are highly susceptible to their environment. The environment in general destroys the quantum nature of the sensor's time evolution in a process called decoherence [126].

From a fundamental point of view, microscopic descriptions of decoherence processes are central to understanding the nature of quantum and classical irreversibility [20, 25, 127–130] and their connection to chaos and thermalization [20, 25, 84, 85, 131–136]. From a more practical side, this relaxation effect plays a highly relevant role in a wide range of processes needed to realize quantum computers [22, 47, 49, 57], quantum simulate or monitor condensed matter many-body systems of interest [20, 21, 25, 59, 60, 63, 86], probe physical, chemical, and biological processes at nanometer scales [21, 23, 24, 27, 63–66, 70, 96, 103, 137], such as protein folding [62, 138–140], and are even the basis of MRI techniques for clinical purposes [24, 70, 115, 125, 141–144].

To successfully achieve such important applications, the key development lies in the ability to suitably control and exploit the decoherence effects. In particular, to move forward with these promising quantum sensing technologies and expand their applicability, it is thus essential to find the best overall strategy to extract the maximum possible information from the environment — either classical or quantum— in the shortest possible time through optimal quantum control and monitoring of the sensor-qubit [93, 137]. This is the main focus of this review.

B. Decoherence control

Conceptually, the idea of considering nuclear spins as sensors through decoherence control is based on identifying the most efficient mechanisms to estimate information through quantum control. The dynamical control tools used to manipulate spins and their decoherence are based on (i) coherent control through electromagnetic irradiation (continuously or pulsed) [41, 43, 44, 49, 75, 76, 145–149] and (ii) incoherent control through projective measurements of quantum states or by stochastic interactions that induce dephasing [50, 53, 150–154].

Coherent control has triggered great interest in the field of quantum information and irreversibility [22, 47, 49, 51, 127, 128, 155–159]. A family of these methods derives from decoupling techniques developed within the NMR field [75, 76, 145–147, 160], that were generalized into what is known as dynamical decoupling (DD) or dynamical control [41, 43–47, 49, 161] to reduce the decoherence effects of quantum states with a serie of time-reversed quantum evolutions. Instead, incoherent control is based on repetitively measuring/projecting a state of a quantum system during its evolution, collapsing the wave function in such a way that one can freeze its dynamics –a phenomenon called the Quantum Zeno Effect (QZE) [162]. In NMR, projective measurements cannot be performed directly, but they can be mimicked by induced dephasing [50, 53, 78, 152, 163].

Although these two control techniques do not appear correlated, their treatment has been unified [43, 44, 164]. This universal approach of quantum control thus forms the basis of modern dynamic control and derives into that either sequences of control pulses, quantum evolutions, or projective measurements effectively modulate the interaction between the system and the environment [21, 23, 24, 43, 44, 49–51, 63, 165, 166].

This modulation of the system-environment interaction is typically represented by a function $f(t)$, where in the case of π-pulse spin-echo sequences [145–147] modulates its effective sign [49]. The square of the Fourier transform of $f(t)$, $F_t(\omega)$, acts as an spectral filter of the environmental noise spectral density $S(\omega)$ [21, 43, 44, 159, 161, 166–168]. Under certain conditions, the decoherence exponentially decays with an argument $\propto \int F_t(\omega)S(\omega)d\omega$ [43, 44, 166]. Thus, in the absence of modulations, the filter $F_t(\omega)$ is centered at zero frequencies, and the corresponding dynamics is dominated by the static components of the environment $S(\omega \approx 0)$. However, the shape of $F_t(\omega)$ changes with control and if the overlap is reduced, the decoherence time increases, while if the overlap increases, the decoherence time decreases. These features schematize the key concepts that are covered in this review: specific spectral or time correlations properties of the environment can be probed to extract relevant information via suitable dynamical control of the qubit-sensor.

C. Decoherence based quantum sensing

In the context of quantum sensing, it is necessary to develop optimal controls of the spins to generate robust filters of the spectral information of the environment [21, 24, 63, 94, 169–171]. In turn, it is necessary to understand what type of information and with what precision can be extracted [93, 137, 172–174]. Combining dynamical control of open quantum systems with quantum information theory and estimation, we have recently shown that there is a maximum extractable information that describe a wide variety of environments characterized by generalized diffusive and relaxation processes [137].

In this short review, we focus on providing the basic and key fundamental concepts and tools that can be used to design proper quantum dynamical control, which instead of increasing decoherence times, highlights or filter in/out specific properties of the environment that are useful for quantum sensing applications (Sec. II). The concepts introduced here are not based on achieving a quantum advantage in processing information compared to classical approaches, but on utilizing real quantum systems that are inherently at spatial scales beyond classical means. These systems can be used to extract either classical or quantum information, potentially leading to novel applications.

To provide context for the key introduced concepts, we present some state-of-the-art examples of these tools being implementated for:

(i) Sensing molecular diffusion processes in NMR and MRI, put into the context of the highly relevant application of quantitative imaging of biological tissue microstructures (Sec. III),

(ii) Probing high-order correlated dynamic of many-body quantum systems using solid-state NMR quantum simulations, with important implications for the development of quantum technologies and the understanding of non-equilibrium quantum physics (Sec. IV), and

(iii) Selectively probing specific interactions via quantum sensors to determine spin-spin coupling-network topologies and therefore molecular structures. It includes strategies relevant for filtering out unknown environment's degrees of freedom and incorporating real time adaptive learning of optimal estimation control (Sec. V).

These concepts are introduced in general terms, so they can be applied to either single or ensemble quantum sensors. We expect that these concepts, which bridge quantum information sciences and technologies with highly relevant applied areas of NMR spectroscopy and MRI, will inspire and facilitate the development of novel mechanisms for monitoring chemical, physical, and biological processes, with particular relevance to non-invasive medical diagnosis.

II. SPIN AS A QUANTUM SENSOR: KEY CONCEPTS

We here illustrate how a generic spin-1/2 I can acts as a qubit sensor of its environment, and its connection to quantum sensing definitions [98], with specific focus on sensing environmental fluctuations that induce decoherence. We thus characterize the decoherence effects induced by the environment, and show how they can be probed by dynamically controlled spin probes. As decoherence effects can be a useful resource of information, we introduce quantum estimation metric tools to extract the relevant information from the environment.

A. Quantum sensing and sensor

According to the definitions reviewed in Ref. [98], quantum sensing is generally based on three strategies: (i) using a quantum system to measure either classical or quantum physical quantities, (ii) utilizing quantum coherence based on a spatial or temporal superposition of states to measure a physical quantity, and (iii) leveraging quantum entanglement to enhance measurement sensitivity or precision beyond classical limits.

The first two strategies involve most of physical systems commonly used at present, having broad applications in various fields. While these strategies do not necessarily utilize quantum information correlations beyond classical metrics, their main advantage over classical sensors is their ability to operate at atomic and

nanoscales, providing information that is inaccessible by classical means [49, 98]. The third strategy offers the additional advantage of entangled quantum systems to achieve Heisenberg-limited measurement [80, 89, 98–100]. However, this strategy is more challenging to implement as it requires multiple sensing qubits to be entangled for then measuring relevant physical quantities for practical applications. In this overview, we focus on the first two quantum sensing strategies that mainly rely on a single qubit-sensor defined by a spin-1/2, and their potential applications.

A quantum sensor such as the spin-1/2 thus is described by two-energy levels and the corresponding eigenstates. It can be initialized in a known-state, manipulated by time-dependent fields and measured at a probing time. The spin-1/2 senses its environment by interacting with physical quantities felt as an effective magnetic field.

In this review, we delve into quantum sensing strategies that involve optimizing the inference of parameters that define essential features of a sensor's environment. Specifically, we focus on how quantum dynamical control, either coherent or incoherent, can aid in this process. Our primary emphasis is on inferring these parameters from steering decoherence effects induced on the spin-sensor due to effective stochastic field fluctuations.

B. Spin dephasing due to the interaction with the environment as a information resource

We consider a spin-1/2 as a quantum sensor for its environment, specifically for detecting effective fluctuating fields induced by the environment through a process known as pure dephasing. The spin state can be initialized into a superposition of its excited ($|\uparrow\rangle$) and ground ($|\downarrow\rangle$) energy states

$$|\psi(0)\rangle = \cos\Theta\,|\uparrow\rangle + e^{-i\phi}\sin\Theta\,|\downarrow\rangle\,, \tag{1}$$

where $|\uparrow\rangle$ and $|\downarrow\rangle$) are the eigenstates of the system Hamiltonian $\mathcal{H}_S = \omega_z I_z$ with I_z the z component of the spin operator. The whole dynamics of the qubit system (S) interacting with its environment (E) is described by the total Hamiltonian

$$\mathcal{H} = \mathcal{H}_S + \mathcal{H}_{SE} + \mathcal{H}_E, \tag{2}$$

where $\mathcal{H}_E$ is the environment Hamiltonian and $\mathcal{H}_{SE}$ is the system-environment interaction Hamiltonian. Single-spin sensors can be typically initialized into this considered pure state, but in magnetic resonance of nuclear spin ensembles, the initial state is describe by a pseudo-pure state [1–4, 8–10, 79, 106]. In the latter case, the spin state is described by the initial density matrix $\rho(0) = p|\psi(0)\rangle\langle\psi(0)| + (1-p)\mathbf{1}$, where $\mathbf{1}$ is the single spin identity operator, and p the probability of creating the state $|\psi(0)\rangle\langle\psi(0)|$ over Boltzmann equilibrium state at infinite temperature defined by $\mathbf{1}$.

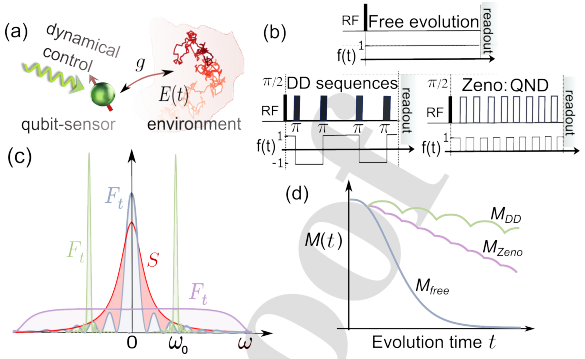

Figure 1. Decoherence control of a quantum sensor. (a) The nuclear spin –a qubit-sensor– can be dynamically controlled to maximize relevant information about its environment coupled by the interaction strength g. This information is inferred by monitoring the induced decoherence caused by the environment fluctuations $E(t)$. (b) Squematic control sequences that modulates the sensor-environment interaction by the function $f(t)$: (i) A free evolution wih a constant $f(t) = 1$. (ii) Spin-echo sequences also called dynamical decoupling (DD) that switch the modulation function sign between $f(t) = \pm 1$. (iii) A free evolution interrupted with projective, quantum non-demolition (QND) measurements. The modulation function is $f(t) = 1$, but at every projective measurement the qubit state resets to its diagonal states and the evolutions starts again from the projected sate. The QZE effect is observed for very frequent QND measurments. All sequences are initiated with a $\frac{\pi}{2}$-excitation RF-pulse and ended by the signal readout. (c) Spectral domain representation of the dephasing. A typical environmental spectral density $S(\omega)$ is shown in red, and the corresponding filters functions $F_t(\omega)$ resulting from the controlled modulations illustrated in (b) are shown in blue (FID), green (DD) and violet (QZE) respectively. The free evolution causes a sinc function centered at 0 frequency, a periodic sequence of inversion pulses produces sincs functions centered at the inverse of the modulating period $\pm\omega_0$, and the QND measurements produces a flat filter that generates the QZE. (d) Schematic behavior of the signal decay of the qubit magnetization $M(t)$ under the three dynamical control shown in (b,c): free (blue), DD (green) and projected evolutions (violet).

We consider the qubit to be subject to environment-induced decoherence, as pure dephasing [49, 175], under the action of the system-environment interaction $\mathcal{H}_{SE} = gI_zE$ (Fig. 1a). Here g is the qubit-environment interaction strength, and E is an environment operator.

On the system rotating frame of reference that precesses at the qubit frequency ω_z, the dynamics of the environment is driven by its Hamiltonian $\mathcal{H}_E$ and seen as a small perturbation on the qubit sensor due to the qubit-environment interaction. By using an interaction representation with respect to the evolution of the isolated environment, we can eliminate the environment Hamiltonian $\mathcal{H}_E$, and the qubit-environment interaction becomes time dependent $\mathcal{H}_{SE}(t) = gI_zE(t)$ with

$E(t) = e^{-i\mathcal{H}_E t} E e^{i\mathcal{H}_E t}$.

A semi-classical field approximation replaces the quantum environment operator $E(t)$ with a stochastic function. We thus simplify its effect as an effective external field fluctuating over time, inducing a spin frequency $\omega_{SE}(t) = gE(t)$ that varies randomly. This typically called weak coupling regime or Born approximation, represents well the quantum qubit-environment interaction up to second order and consider negligibly the qubit-sensor influence on the environment [43, 44, 166, 175–179]. Under this approximation, even if the environment is quantum, the interaction is effectively modeled by a fluctuating classical field. As a result, the quantum sensor infers classical information from the environment. However, this classical information can reveal physical properties at atomic or nanoscale that might not be accessible by classical sensors.

Considering an ensemble of realizations of this random noise on the qubit system means that the average magnetization vector differs from the individual evolutions. This average magnetization represents an ensemble average of non-interacting, equivalent spins as in bulk NMR, or the ensemble average of the quantum evolutions of a single spin-sensor. Then, the spin magnetization signal $M(t) = Tr[\rho_S(t) I_x] = \langle I_x(t) \rangle$ of the x spin operator component, gives the observable of the mean spin coherence

$$M(t) = \left\langle e^{-i\phi(t)} \right\rangle M(0). \tag{3}$$

The phase acquired by a spin during the evolution time t, is $\phi(t) = \int_0^t \omega_{SE}(t')dt'$, and the average over the random phases of the spin ensemble is denoted by the brackets. Under dynamical control with spin-echo sequences [49, 145–147], the average phase becomes null, $\langle \phi(t) \rangle = 0$. Typically the random phase $\phi(t)$ follows a Gaussian distribution [180], and the spin signal

$$M(t) = e^{-\mathcal{J}(t)} M(0) \tag{4}$$

thus depends on its random phase variance via the attenuation factor $\mathcal{J}(t) = \frac{1}{2} \langle \phi^2(t) \rangle$ [49]. For single spin sensors [27, 30, 65, 90, 91, 96, 103, 158, 181–184], this characteristic decay is inferred from the probabilities $p_\pm(t) = \left(1 \pm e^{-\mathcal{J}(t)}\right)/2$ of measuring the system in the symmetric or antisymmetric superpositions of energy states, $|\pm\rangle = |\uparrow\rangle \pm |\downarrow\rangle$ [137].

C. Probing environment correlation functions and noise spectrum by dynamical control

We here introduce how information from the environment is manifested by time correlation functions and/or their corresponding spectral representations, on the pure dephasing effects experienced by the spin-1/2 sensor. We also show, how to probe this information by dynamically controlled qubit-sensors.

Under the considered weak-coupling regime between the qubit and its environment, the decoherence attenuation factor of the qubit-sensor state is expressed by the integral product (overlap) of two functions [43, 44, 166]: the coupling spectrum of the environment $S(\omega)$ that is obtained by the Fourier transform of the autocorrelation function of the qubit-frequency fluctuation induced by the environment $\langle \omega_{SE}(t) \omega_{SE}(t') \rangle$, and a spectral "filter" function $F_t(\omega)$ determined by the Fourier transform of the modulating function $f(t)$ of the applied control.

As schematized in Fig. 1b, the quantum dynamical control may be coherent, incoherent, continuous or pulsed, and it modulates effectively the qubit frequency as $f(t)\omega_{SE}(t)$ [49]. Under free evolution, $f(t) = 1$ for the whole time interval, while under coherent control, it may be arbitrarily modulated. In particular, for a serie of inversion π-pulses (spin-echo sequences [145–147]) applied to the qubit by electromagnetic fields, the control modulating function switches between ± 1 at every instant where the instantaneous pulses are applied [49, 161]. An incoherent control may be applied by quantum non-demolition (QND) projective measurements [137] and/or induced dephasing mimicking the QND measurement [50, 53, 78, 79, 152], that repetitively and stroboscopically projects the qubit state, for example to its initial state. Here, the control modulating function is $f(t) = 1$ following a free evolution until the next measurement/projection, where the qubit phase is reset to its initial value and the qubit evolution starts again [43, 44, 151, 177]. When it is done frequently, it freezes the dynamics evoking the QZE [162].

The control parameters may be the total evolution time t, the number of pulses or modulating oscillations N, etc. For simplicity, in the following, we leave those parameters implicit and will explicit only some of them when it is required. Under these considerations, the attenuation factor $\mathcal{J}(t)$ of Eq. (4), characterizing the magnetization decay, becomes

$$\mathcal{J}(t) = \frac{1}{2} \int_0^t dt' \int_0^t dt'' f(t') \langle \omega_{SE}(t') \omega_{SE}(t'') \rangle f(t''), \tag{5}$$

where in several situations the correlation function is stationary $\langle \omega_{SE}(t') \omega_{SE}(t'') \rangle = \langle \omega_{SE}(0) \omega_{SE}(t'' - t') \rangle$ and gives the frequency domain representation

$$\mathcal{J}(t) = \int_{-\infty}^{\infty} F_t(\omega) S(\omega) d\omega. \tag{6}$$

Figure 1c shows the filter functions $F_t(\omega)$ corresponding to the control modulations shown in Fig. 1b, while the associated corresponding magnetization decays are shown in Fig. 1d. The filter property of the modulating control of the qubit frequency can be seen as, if $F_t(\omega)$ is 1, it passes the experimental noise at that frequency without attenuation whereas if it is 0, it blocks the noise completely at that frequency. By suitable design of quantum control strategies, one can tune up the "filter" func-

tion to successfully complete a specified task in the presence of the environment [56, 93, 137, 161, 166, 168, 185–187]. In particular one can exploit this filter function description for quantum sensing the environment spectral density, in a process called noise spectroscopy [49, 98]. Based on dynamical decoupling or spin-echo train sequences, it consists of changing the filter function $F_t(\omega)$, *e.g.*, by varying π-pulse spacing or the control-field Rabi frequency, recording the resulting decoherence decay $\mathcal{J}$ to deduce the noise spectral density $S(\omega)$ [21, 63, 165, 166, 179, 188, 189]. Alternative approaches are based on relaxometry, a term originated in magnetic resonance spectroscopy for measuring relaxations times as a function of a magnetic field strength [176, 190, 191]. It uses perturbation theory and the Fermi's golden rule to probe specific frequency components of the spectral density by changing the magnetic field strength.

We focus here on probing decoherence effects based on the expression Eq. (6) by dynamical quantum control with pulse sequences. Remarkably, Eq. (6) applies not only for pure dephasing effects under coherent and incoherent control as we focus here, but also for dissipation effects [44, 137, 173, 177]. Moreover, it is still valid for non-stationary noises based on identifying the non-stationary environmental eigenmodes as recently demonstrated in Ref. [166].

Notice that for presentation purposes, we consider only one term in the qubit-environment interaction, however, the framework considered in this section can be extended to multiple environment interactions $\sum_i g_i S_i E_i$ by representing $S(\omega)$ and $F_t(\omega)$ as matrices [166, 168, 186, 192]. Typical shapes for the environmental, noise spectral density $S(\omega)$ are for example the Ohmic power law in ω, a Lorentzian function representing an Ornstein-Uhlenbeck process, and generalizations of them as the inverse of a polynomial of the frequency ω [21, 24, 137, 166, 193–195] as it is the case of a quantum brownian motion for example [175] For non-stationary environments, a bispectrum or multiple frequency dependences enter into account [166, 187] and more complex multi-spectrums need to be considered for non-Gaussian noises [170, 179].

D. Inferring environmental parameters and attaining their ultimate error bounds by dynamical control

In this section we introduce information metrics that can be exploited to optimize the quantum sensing control strategies for inferring specific parameters that characterize some property of the qubit-sensor's environment. Probing the environmental spectral density by noise spectroscopy methods typically requires several measurements to reconstruct fully $S(\omega)$ [21, 63, 179] However, if the functional form of the noise spectrum is known, one may only probe specific parameters that describe the noise spectrum [24, 66, 92, 93, 137, 196]. In this case, the figure-of-merit for the estimation of an environmental parameter x_E that characterizes the environment of the sensor is its relative error $\varepsilon = \frac{\delta x_E}{x_E}$.

The relative error ε of the parameter extracted from the magnetization signal of Eq. (4), is limited by the quantum Cramer-Rao bound ε_{CR} for an unbiased single-parameter estimation [98, 137, 197–199],

$$\varepsilon \geq \frac{\varepsilon_{CR}(x_E)}{\sqrt{\mathcal{N}}} = \frac{1}{x_E\sqrt{\mathcal{N}\mathcal{F}_{\mathcal{Q}}(x_E)}}. \tag{7}$$

Here ε_{CR} defines the minimal attainable relative error per measurement $\mathcal{N}$. It is written as a function of the quantum Fisher information (QFI) $\mathcal{F}_{\mathcal{Q}}(x_E)$ of the parameter x_E [137, 197, 198].

The QFI depends on the behaviour of the spin magnetization signal in Eq. (4) [137, 173, 198, 200] with a functional dependence on the parameter to be estimated x_E, the total evolution time t of the decaying signal and the control parameters, according to the equation

$$\mathcal{F}_{\mathcal{Q}}(x_E) = \sin^2(2\Theta) \underbrace{\frac{\left[\frac{M(t,x_E)}{M(0)}\right]^2}{1-\left[\frac{M(t,x_E)}{M(0)}\right]^2}}_{\text{amplitude contrast}} \underbrace{\left(\frac{\partial \ln\left[\frac{M(t,x_E)}{M(0)}\right]}{\partial x_E}\right)^2}_{\text{parametric-sensitivity}} \tag{8}$$

Then, by maximizing $\mathcal{F}_{\mathcal{Q}}$ with respect to the dynamical control parameters, the minimum relative error ε_{CR} is minimized [137, 199]. Therefore the optimal control parameters defined by

$$\mathcal{F}_{\mathcal{Q}}^{\text{opt ctrl}}(x_E) = \max_{\text{ctrl}}(\mathcal{F}_{\mathcal{Q}}(x_E)), \tag{9}$$

provides the minimum attainable error $\varepsilon_{CR}^{\text{opt ctrl}}(x_E)$ for each chosen control, based on preparing the optimal initial state (1) with $\Theta = \frac{\pi}{4}$, and achieving the best trade-off between the amplitude contrast of the qubit signal and its parametric-sensitivity to x_E according to Eq. (8) [137, 199].

When the spectral density has a frequency range with a power law dependence on the parameter to be estimated, suitable control can be designed to filter in this frequency modes thus giving $\mathcal{J} \propto x_E^{\pm\alpha}$. Then, it is demonstrated that there exist an ultimate error bound in the estimation per measurement that applies to *all* possible control sequences

$$\varepsilon_{CR}^{\text{opt ctrl}} \geq \frac{\sqrt{1-e^{-2\mathcal{J}_0}}}{\alpha\,\mathcal{J}_0\,e^{-\mathcal{J}_0}} = \frac{\varepsilon_0}{\alpha}, \tag{10}$$

but remarkably it is only attainable under suitable control [137]. Here the value of $\mathcal{J} = \mathcal{J}_0 = 1 + \frac{1}{2}W(-2e^{-2}) \approx 0.8$ that minimizes this bound, where $W(z)$ is the Lambert function, yields the equality with $\varepsilon_0 \approx 2.48$.

The optimal control designed to attain this ultimate relative-error bound ε_0/α for key environmental parameters x_E should thus probe the regime $\mathcal{J} \propto x_E^{\pm\alpha}$ at a time such as $\mathcal{J} = \mathcal{J}_0$. Examples of such key parameters are the coupling to the environment g, the correlation time

τ_c, diffusion coefficients D_0, and the relaxation time T_2 among others [24, 66, 73, 93, 137, 196, 199].

Notice that the attained ultimate precision bound discussed in this section, gives the standard quantum limit, as the inference strategy is based on a single-qubit sensor paradigm [98, 198]. This precision limit thus can be improved if multi-qubit sensors are implemented to exploit entanglement for reaching the Heisenberg-limit [80, 89, 98–100].

Summary: Selective and optimized inference of environmental parameters

The basic and key concepts presented in this section show how dynamically controlled qubit-probes can highlight or filter in/out environmental modes. Quantum control can thus steer decoherence to probe specific information on the environment, rather than reducing its detrimental effects. We address the challenge of extracting efficiently the relevant information for specific purposes, as full knowledge in practical times is not possible. We introduce quantum information metrics and quantum control strategies for maximizing the extractable environmental information.

III. PROBING MOLECULAR DIFFUSION PROCESSES: TOOLS FOR CHARACTERIZING TISSUE MICROSTRUCTURE

In this Section, we show how the presented general tools can be use to extract highly relevant tissue microstructure information from the noise correlation functions via the dephasing of the qubit-probes in diffusion weighted NMR-MRI [107, 108, 110, 111]. We first introduce the principles that characterize the spin dephasing induced by the molecular displacement due to Brownian motion in presence of a constant magnetic field gradient, and then demonstrate two important applications of these concepts. The combination of quantum estimation metrics and quantum control tools predict the ultimate precision limits for estimating tissue microstructure sizes, and they enable selective inference of specific microstructure sizes.

A. Decoherence induced by molecular displacement noises

In diffusion-weighted magnetic resonance spectroscopy and imaging, the nuclear spins of molecules intrinsic to biological tissues and porous media in general, in particular the spins 1/2 of protons in water molecules, interact with external magnetic field gradients along their random Brownian motion [77, 115, 119]. Properties of the media microstructure are indirectly codified in such

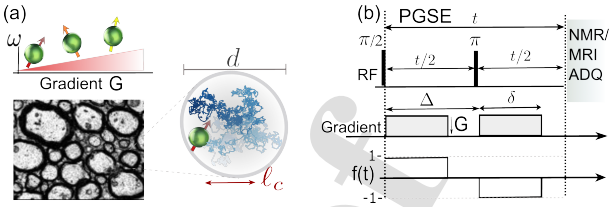

Figure 2. Concepts of diffusion-weighted NMR/MRI signals for probing tissue microstructure sizes. (a) Schematic image of axon diameters in the brain white matter. The myelin sheath covers them (dark circles) to protect the nerve and communication of the central nervous system. In presence of a constant magnetic field gradient, nuclear spins precesses with different frequencies at different spatial positions. A Brownian motion of the nuclear spins is schematized highlighting how they can probe restriction length of the diffusion process ℓ_c, associated with microstructure sizes, e.g. in a cylindrical compartment $\ell_c = 0.37\,d$, where d is the diameter. (b) Pulse Gradient Spin Echo (PGSE) sequence for probing the diffusion correlation length: An initial $\frac{\pi}{2}$-excitation RF pulse, followed by the diffusion weighting contrast building block that consists of a π-pulse at half the diffusion weighting time t and ended by the signal readout. In between two gradient pulses of duration δ, with Δ as the delay between the two gradient pulses. When $\delta = \Delta = \frac{t}{2}$, PGSE is equivalent to a Hahn gradient modulation sequence.

interaction. The media structure can affect the magnetization signal and its decay through various physical processes. The relaxation times T_1 and T_2, for example, are impacted by compartment sizes due to changes in the mobility of water molecules near compartment walls [77, 201–205]. Additionally, magnetic susceptibility heterogeneities can induce inhomogeneous fields, which are often referred to as background or internal gradients [92, 196, 203, 206–213]. Finally, compartment restrictions can also influence the Brownian motion of spin-bearing particles [24, 66, 110, 214–220]. All these features are thus useful to extract microstructure properties beyond the resolution limits imposed by conventional MRI acquisition. However, obtaining this information typically requires implementing suitable dynamical control over spin decoherence effects.

Our focus here is solely on extracting information regarding the size of tissue or porous microstructures from the decoherence effects that occur in the spin signal due to the restricted Brownian motion of molecules within the compartments of the media (Fig. 2a) [110, 115, 119, 216, 221]. This sets a simple paradigmatic example, where suitable probing specific properties of the diffusion spectral density based on the concepts introduced in the previous section, provides quantitative information about microstructure sizes [24, 66, 70, 120, 220]. In some cases, T_1 and T_2 relaxation weightings can be factored out from the signal [24, 66], and internal gradients effects can also be vanished by suitable design of the pulse sequences symmetries [92, 203, 222, 223].

We consider the sample in presence of a static mag-

netic field. The Larmor precession frequency of the spins is defined by a homogeneous magnetic field along the z axis. We describe the magnetization evolution of spins diffusing within the compartments in the rotating frame of reference at this Larmor frequency. Then in presence of uniform magnetic-field gradient $G\hat{r}$ applied along an arbitrary direction $\hat{r}$, the precession frequency of the spins $\omega_{SE}(t) = \gamma\vec{G}\cdot\vec{r}(t)$ fluctuates due to the spin's instantaneous position $\vec{r}(t)$ suffers a random motion, where γ is the gyromagnetic factor of the corresponding nucleus [77, 224]. As typically the random phase $\phi(t)$ accumulated by the spins during a diffusion time t is describe by a Gaussian phase distribution [225], the spin dephasing given by Eqs. (4) and (5), depends of the molecule displacement autocorrelation function $\langle\omega_{SE}(t')\omega_{SE}(t'')\rangle = \gamma^2G^2\langle\Delta r(t')\Delta r(t'')\rangle = \gamma^2G^2\langle\Delta r(0)\Delta r(t'-t'')\rangle$. The brackets represent the ensemble average over the random phases and $\Delta r(t) = r(t) - \langle r(t)\rangle$ is the instantaneous deviation of the spin position from its average value [218, 219].

For molecules that diffuse within the media microstructure, the displacement autocorrelation function contains information about the boundaries of the compartment where the molecules are contained [24, 66, 70, 93, 94, 114–118, 120, 121, 123, 124, 226–228]. For example a simple model for restricted diffusion is the Ornstein-Uhlenbeck process, where $\langle\Delta r(0)\Delta r(t-t')\rangle = D_0\tau_c e^{-|t-t'|/\tau_c}$ with D_0 the free diffusion coefficient and τ_c the correlation time [24, 66, 180, 216]. The characteristic time τ_c is the one required on average for a molecule to probe the boundaries of the compartment characterized by the restriction length ℓ_c, which are related by the Einstein's law $\ell_c^2 = 2D_0\tau_c$ [77]. The Fourier transform of this autocorrelation function thus gives the displacement spectral density [24, 66, 93, 216, 218],

$$S(\omega) = \frac{\gamma^2G^2D_0\tau_c^2}{\pi(1+\omega^2\tau_c^2)} = \frac{\gamma^2G^2D_0\ell_c^4}{\pi(4D_0^2+\omega^2\ell_c^4)}. \quad (11)$$

Modulated gradient spin echo (MGSE) sequences generates time dependent magnetic field gradient $G(t) = f(t)G$, yielding the spectral filter $F_t(\omega)$ that is used to probe the displacement spectral density related with the diffusion spectrum as $D(\omega) = \omega^2S(\omega)/\left(\gamma^2G^2\right)$ [66, 77, 119, 216, 221]. With this, the corresponding attenuation factor described by Eq. (6) can be calculated.

In a restricted diffusion process due to a close (non-permeable) compartment, the restriction length ℓ_c depends on the geometric size and shape of the compartment [216, 229, 230]. For the examples of simple geometries as spheres, cylinders, or planes, a good approximation is given by $\ell_c = \sqrt{2}\chi d$ with χ =0.21, 0.26, and 0.30, respectively with d the sphere and cylinder diameter or the plane distance, respectively [24, 66, 216, 219]. Figure 2a shows a scheme of the relation of the restriction length of the Brownian motion with the diameter of a cylinder.

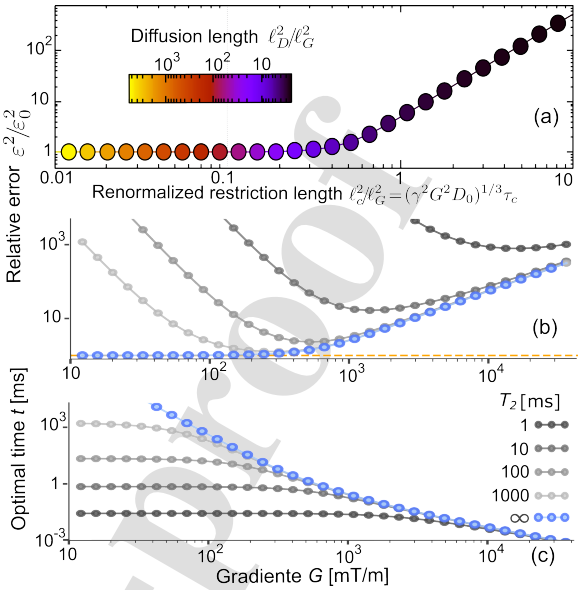

Figure 3. Attaining the ultimate precision bound of the restriction length ℓ_c from diffusion-weighted magnetization decays. (a) Relative minimum error $\varepsilon^2/\varepsilon_0^2$ per measurement as a function of the normalized restriction length ℓ_c^2/ℓ_G^2 for the estimation of ℓ_c. The colored scale for the circles gives the normalized optimal diffusion length ℓ_D^2/ℓ_G^2. The bound is approached when $\ell_c^2/\ell_G^2 \ll 1$ and $\ell_D^2/\ell_G^2 \gg 1$, and $\frac{\ell_c^4\ell_D^2}{\ell_G^6} = \mathcal{J}_0$, implying $\left(\gamma^2G^2D_0\right)^{1/3}\tau_c \ll 1$. The quantity $\varepsilon^2/\varepsilon_0^2$ yields directly the number of measurements $\mathcal{N}$ needed to attain the ultimate precision bound per measurement. (b,c) Effects of T_2-relaxation on the estimation of $\ell_c = 0.37d$ for a cylindrical compartment diameter of $d = 5\mu$m with a diffusion coefficient $D_0 = 1\mu\text{m}^2/\text{ms}$ representative to brain gray/white matter. Relaxation times $T_2 = 1000, 100, 10, 1$ms (light to dark gray circle-lines) are considered and contrasted to the case without T_2 effects (blue circle-line, equivalent to $T_2 = \infty$). (b) Relative error $\varepsilon^2/\varepsilon_0^2$ in the estimation and (c) the corresponding optimal time t, as a function of the gradient strength G for the optimized PGSE control sequence ($\delta = \Delta$). As shorter is T_2, more detrimental are its effects on the precision in the estimation of d, and reduces the dynamic range of gradients that can attain the best performance.

B. Precision Limits of Compartment Microstructure-Sizes

Resorting to the information estimation tools introduced in Sec. II D, we can now define the optimal control strategy to attain the ultimate error bound per measurement defined in Eq. (10), to estimate the restriction length parameter $x_E = \ell_c$ and thus compartment size information [93, 137]. The MGSE control sequence should be such that $f(t)$ satisfies the following requirements: *(i)* Its spectral filter $F_t(\omega)$ should only overlap with the displacement power spectrum $S(\ell_c, \omega)$ (Eq. (11)) within the spectral region with the strongest dependence on ℓ_c to enhance the estimation sensitivity, i.e. at low frequencies

when $S(\ell_c, \omega \approx 0) \propto \ell_c^4$. Within this regime, the signal attenuation factor is $\mathcal{J}(t) \propto \ell_c^4$, and thus has a power law dependence on the parameter to be estimated, ℓ_c, allowing to use Eq. (10) with $\alpha = 4$. *(ii)* The total diffusion time t should be such that $\mathcal{J} = \mathcal{J}_0$ as predicted by Eq. (10).

Based on these arguments, a MGSE control sequence that produces a narrow low-frequency bandpass filter thus defines the strategy most sensitive to infer the restriction size ℓ_c. The most typical sequence used in diffusion weighting imaging is the Pulse Gradient Spin Echo (PGSE) [77, 231], which contains only one gradient-sign switch as shown in Fig. 2b. The longest possible modulation period is when $\delta = \Delta = \frac{t}{2}$, and thus if optimized gives the narrowest low-frequency bandpass filter, analogously to the one of a Hahn spin echo sequence [145] with a constant gradient or a gradient echo modulation [93]

$$F^{PGSE}_{\delta=\Delta=\frac{t}{2}}(\omega) = t^2 \mathrm{sinc}^2\left(\frac{\omega t}{4}\right)\sin^2\left(\frac{\omega t}{4}\right) = F^{Hahn}_t(\omega). \tag{12}$$

The condition *(i)* to attain the bound is then satisfied if the diffusion time is $t \gg \tau_c$ with the corresponding attenuation factor

$$\mathcal{J}(t) = \frac{\gamma^2 G^2}{4D_0}\ell_c^4 t. \tag{13}$$

From the requirements (i)-(ii), we thus found [93] that the optimal diffusion time is

$$t = 4D_0\mathcal{J}_0 / \left(\gamma^2 G^2 \ell_c^4\right). \tag{14}$$

In Fig. 3a we show the optimized relative error determined from this optimized diffusion time as a function of the restriction length ℓ_c and the diffusion length $\ell_D = \sqrt{2D_0 t}$ in units of the dephasing length $\ell_G = \sqrt[3]{\frac{2D_0}{\gamma G}}$ [77, 93]. The ultimate bound is only attained for $\ell_c \ll \ell_G \ll \ell_D$[93].

The optimal diffusion length increases with reducing the restriction length, thus under experimental conditions when T_2 relaxation becomes relevant, the ability to achieve this optimized diffusion time is limited by the intrinsic decoherence effects that decrease the magnetization signal by $M_{T_2}(t) = e^{-\frac{t}{T_2}}M(t)$. Then the relative error bound exponentially increases with $\frac{t}{T_2}$ [93]

$$\varepsilon \geq e^{\frac{t}{T_2}}\varepsilon_0. \tag{15}$$

Accounting thus for different T_2 relaxation times, Figure 3b shows the optimized relative error, and Fig. 3c the corresponding optimal diffusion time t, for a restriction length defined by a cylinder with diameter $d = 5\mu$m as a function of the gradient strength used for the optimized PGSE sequence. There is now an optimal gradient strength for a given T_2 time, that increases with decreasing T_2. Also as predicted by Eq. (15), the lower attainable relative error increases with reducing the T_2 time.

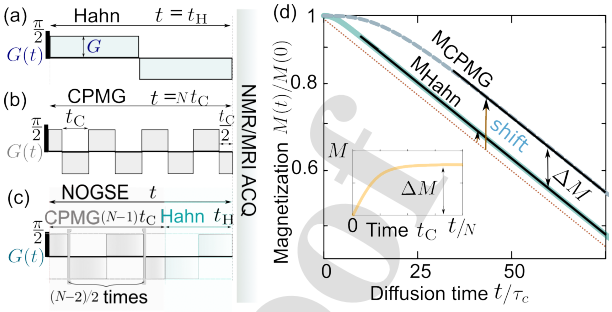

Figure 4. Decay shifts for probing selective microstructure sizes. MGSE sequences: (a) Hahn gradient modulation shape, (b) periodic modulations as in CPMG or OGSE, and (c) NOGSE. They start with an excitation $\pi/2$-pulse followed by modulated gradients and end with an MRI acquisition protocol. The NOGSE sequence concatenates the Hahn (a) and CPMG (b) gradient modulations with a total of N refocusing periods during $t = (N-1)t_C + t_H$. (d) Spin-echo magnetization decay for the Hahn and CPMG modulations as a function of the diffusion time t/τ_c. For refocusing periods $t_C \gg \tau_c$ and $t_H \gg \tau_c N$, the decay-rate is constant $\gamma^2 G^2 D_0 \tau_c^2$ (black solid line). The shift from the free-evolution decay (dashed) increases with N. The contrast ΔM between both sequences is selectively probed by the NOGSE by changing the ratio between t_C and t_H for a fixed t (inset).

Notice that the results presented in this section, assume that other experimental errors during the acquisition of the spin signal are lower than the quantum state uncertainty. Further considerations similar to those evaluated for T_2 relaxation limitations might need to be taken into account as well. The optimization of control will, therefore, depend on these additional sources of uncertainty. Nevertheless, the precision bounds predicted here are the ultimate ones that can be attained if the introduced sensing protocol is performed. We find that this bound can be improved, and recalculated, by modifying the PGSE sequence using stimulated echoes [232], that store the magnetization signal on the z-axis during the delay Δ to avoid the T_2 relaxation mechanisms, and extend the signal lifetime to T_1 relaxation times. The considered precision bounds are dictated by the standard quantum limit. Recently, it was introduced the use of NOON state preparation in multi-spin molecules for a more sensitive probe of molecular diffusion that improves the considered precision bound [233].

C. Probing selective microstructure-sizes with spin-echo decay-shifts

Typically the decay of the spin-echo magnetization as a function of the diffusion time, is reduced by increasing the gradient oscillation frequency of the refocusing periods of MGSE sequences (Fig. 4) [24, 66, 119, 218, 219]. However, within the restricted diffusion regime, when the

refocusing periods are longer than the correlation time τ_c, the dephasing cannot be refocused as the spins have fully explored the restricting compartment. The spin-echo decays exponentially with the attenuation factor

$$\mathcal{J}(t) = \gamma^2 G^2 D_0^2 \tau_c^2 \left(t - (2N+1)\tau_c\right) \tag{16}$$

for square gradient modulations [24, 66, 94]. The attenuation factor thus has a constant rate $\frac{d\mathcal{J}(t)}{dt} = \gamma^2 G^2 D_0^2 \tau_c^2$ that is independent of the number of refocusing periods N (black solid line in Fig. 4d). As the transition from the free-diffusion to the restricted regime depends on the modulation periods, even at long times this information remains in the spin-echo as a "decay-shift" (see Fig. 4b) [24, 66, 94, 234]

$$\gamma^2 G^2 D_0 \tau_c^3 (2N+1) \propto \ell_c^6. \tag{17}$$

Due to this shift, subtracting spin-echo signals derived from MGSE sequences with different numbers of modulating periods still gives a non-null signal reflecting a contrast directly proportional to the restriction length as $\propto \tau_c^3 = \ell_c^6$ [24, 66]. Thus this provides a selective probe of microstructure restriction sizes that can be directly reflected on the image contrast [94]. Moreover, the decay shift has a parametric sensitivity to the restriction length of a power of 6, compared to a power of 4 if the restriction size is determined from the width of the displacement power spectrum of Eq. (11), which can be determined from the spin-echo decay-rate.

This decay-shift can be selectively probed by a Non-uniform Oscillating Gradient Spin Echo (NOGSE) sequence (Fig. 4c) [24, 66], which is also advantageous to avoid other relaxation mechanisms to keep the total diffusion time constant as well as the number of sign switches of the gradient that introduce imperfections. Internal gradient effects can also be removed by suitable designing NOGSE sequences with time modulation symmetries that cancel out those effects [92]. The sequence was inspired by non-uniform spin-echo sequences introduced within the quantum information processing community [23, 46, 143], and it is based on concatenating two gradient modulation sequences with different frequencies, one with one refocusing period t_H and the second with $N-1$ refocusing periods t_C [24, 66]. Then, by changing the ratio between their corresponding refocusing periods such that the total diffusion time is $t = (N-1)t_C + t_H$, the contrast between the extremes can be probed (Inset of Fig. 4b).

In the regime of restricted diffusion, the NOGSE contrast ΔM reflects the difference between two MGSE sequences with different gradient frequency modulations [24, 66, 94]

$$\Delta M \approx e^{-\gamma^2 G^2 D_0 \tau_c^3 (\frac{t}{\tau_c} - 3)} \left(e^{\gamma^2 G^2 D_0 \tau_c^3 2(N-1)} - 1 \right), \tag{18}$$

where we have subtracted the spin-echo signal between the refocusing-period limits when $t_C = t_H$ and when $t_C \to 0$, $t_H \to t$.

If the restricted diffusion regime is reached with a restriction diffusion length small compared to the dephasing and diffusion lengths, $\ell_c \ll \ell_G \ll \ell_D$, then, the NOGSE contrast ΔM can be approximated by a Gaussian function as a function of ℓ_c [94]

$$\Delta M \approx 2(N-1)e^{-3/2} \left(\frac{\ell_c^f}{\ell_G}\right)^6 \exp\left[-12\left(\frac{\ell_c - \ell_c^f}{\ell_c^f}\right)^2\right], \tag{19}$$

where the maximum contrast is attained for a restriction length $\ell_c^f \approx \sqrt[4]{\frac{3}{2}}\sqrt{\frac{\ell_G^3}{\ell_D}}$. Thus this demonstrates how the NOGSE contrast acts as a microstructure-size "bandpass-filter" [94]. The maximum of ΔM at the size ℓ_c^f can be tuned to highlight a given restriction length ℓ_c if the media contain compartment size distributions, by choosing properly the sequence control parameters, i.e. the gradient strength G and the diffusion time t.

Figure 5 shows proof-of-principle MRI experiments that were performed in the Corpus Callosum of an ex-vivo mouse brain [94, 235]. Two images of the Corpus Callosum, based on the contrast ΔM of a NOGSE sequence for two gradient strengths are shown. The signal originating from water diffusing in smaller restriction lengths gives a stronger contrast signal for the larger gradient, and the one originating in larger restriction lengths is manifested on the image with a weaker gradient.

Two region-of-interest (ROI) are marked, and their averaged signal is shown in Fig. 5b as a function of the gradient strength. As the biological tissue microstructure is heterogeneous, to fit the experimental data we assume an established log-normal distribution model $P(\ell_c)$ for the compartment sizes. Then, the observed contrast is the contribution of signals originated from all the compartments weighted by the log-normal distribution $\Delta M = \int_{\ell_c} P(\ell_c)\Delta M(\ell_c) d\ell_c$. From the fitting we extract the size distributions shown in Fig. 5c. The Figure also shows the expected signal contrast ΔM as a function of the restriction length for the two gradient strength used in Fig. 5a.

The colored contrast shown in Fig. 5a without assuming any distribution size model is consistent with the size distributions determined in Fig. 5c, where the corresponding NOGSE filters that overlap on them, highlight ROI 1 for the larger gradient as smaller sizes are probed comparing with the ROI 2 size-distribution. Instead, ROI 2 is highlighted for the weaker gradient, as it contains larger sizes than the ones in ROI 1. These results are consistent with histological validations [220]. The NOGSE ability to generate contrasts based on selective signals originating from specific microstructure sizes is thus demonstrated [94].

Summary: Towards non-invasive histology of tissue microstructures

A great challenge faced by diffusion weighting imaging, is how to extract detailed tissue microstructure features

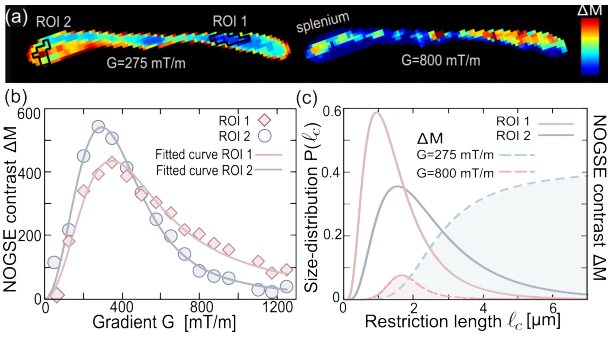

Figure 5. NOGSE contrast images of selective microstructure sizes in an ex-vivo mouse brain. (a) Images of the Corpus Callosum of an ex-vivo mouse brain were performed on a Bruker Avance III HD 9.4T WB NMR spectrometer, based on NOGSE contrast ΔM fixing G, $N = 2$ and $t = 21.5$ ms [235]. (b) Average ΔM signal as a function of G for the two ROIs marked in (a). Our theoretical model for a log-normal distribution fit the experimental data with median 1.34 ± 0.04 and 2.22 ± 0.02 μm and geometric standard deviation 1.82 ± 0.02 and 1.82 ± 0.02 μm for ROI 1 and ROI 2 respectively, considering $D_0 = 0.7$ μm^2/ms. (c) The size-distribution $P(\ell_c)$ and ΔM as a function of ℓ_c for the ROIs and G indicated in (a).

as a non-invasive "histology" mechanism. These microscopic details are relevant for understanding pathology mechanisms and developing treatments of cancer and neurodegenerative diseases. Attaining this goal sets a highly relevant challenge, where NMR and MRI quantum technologies play an important role. Quantitative information on tissue microstructure needs to be extracted fast and reliably, as in-vivo imaging imposes hard constraints on image acquisition times.

Towards achieving those goals, this section thus shows how quantum information metrics can help designing suitable electromagnetic pulse sequences to extract quantitative information of tissue microstructure sizes. The extractable information is bounded by fundamental quantum physics limits that give a tool to asses when quantitative information can be extracted reliably and in practical times. While the methods consider estimating compartment restriction sizes, they are general and can be adapted to different settings and relevant parameters. Achieving optimal strategies for extracting the relevant information, depends on model knowledge that characterizes the tissue microstructure. Towards developing tools to extract information without this prior knowledge, we demonstrate how suitable dynamical control can filter in the signal of selective compartment-sizes. This approach is independent of size distribution assumptions. It thus sets a step towards designing methods to scan size distribution, by tuning control parameters of MRI sequences.

IV. PROBING MANY-BODY QUANTUM SYSTEMS OUT OF EQUILIBRIUM: TOOLS FOR CHARACTERIZING THE DYNAMICS AND SCRAMBLING OF QUANTUM INFORMATION

In this Section, we provide tools for evaluating the reliability of controlling the quantum dynamics of many-body systems with time reversal echo sequences. As realistic operations intrinsically contain imperfections, we thus show how to quantify the fragility of a controlled dynamics to perturbations by monitoring decoherence effects of suitable designed sequences. We first consider the dynamics of quantum information on these large systems, and show how it is connected to quantum information scrambling, a kind of "quantum spin diffusion" process. We show how this complex dynamics is determined by Out-of-Time-Order Correlations (OTOCS) that can be measured with multiple quantum coherences. We introduce time reversal echo sequences that can determine the fidelity of the control dynamics of quantum information, and show how it is determined by the effective number of active spins involved on the quantum evolution. Finally, we show how the fragility of quantum dynamics intrinsically depends on the number of correlated active spins that quantify a "quantum diffusion" coherent length.

A. Quantum spin diffusion and information scrambling

Quantum control to generate generalized time reversal echoes [127, 236, 237] similar to the spin-echo concept, can also be used to probe the "quantum diffusion" process on spin-coupled networks in solid state systems. In this case, rather than probing the spins spatially moving, their excitations exchange between different spin sites quantum mechanically (Fig. 6) [238, 239]. The latter was demonstrated as its quantum evolution is reversible in time [127, 236, 237].

This spin dynamic leads to the build-up of many-body quantum superpositions. Initially, they were measured within NMR by observing multiple quantum coherences (MQC) using spin counting techniques [240–246] MQCs provide a hard lower bound on the number of correlated spins, allowing us to predict the propagation of a local excitation within a spin network [20, 25, 83–85, 136, 247–250]. MQCs are a useful tool because they are relatively easy to measure and characterize without requiring a full quantum state tomography, which is impossible on practical times for large quantum systems.

MQC experiments, typically begin with an initial state in which the spin states involve local information, because they are uncorrelated on the Boltzmann equilibrium. The quantum mechanical propagation of this local information into many degrees of freedom describes what we call a "quantum diffusion process" (Fig. 6), also known as *quantum information scrambling* because the complex correlations created on many-body states

prevents information from being extracted from local measurements [136, 251–253]. Recently, it has been demonstrated that scrambling dynamics can be characterized by MQC [20, 25, 86, 248, 249, 254], and observing these dynamics has become a significant area of study [136, 253]. MQC have a well-established history in solid-state NMR systems, which typically operate at high temperatures [20, 25, 240–246]. However, advancements in cold-atom experiments now make it possible to measure MQCs in nearly pure, zero-temperature initial states [136, 248, 249]. Undestanding the scrambling dynamics is shedding light to outstanding problems in various disparate physics fields from quantum statistical mechanics to cosmology [136, 253], including quantum chaos [82, 86, 250, 255, 256], irreversibility [20, 25, 85, 86, 247, 254, 257], thermalization [25, 59, 84, 247, 258] and entanglement [136, 249].

Here, we provide an overview of the connection between tools developed within solid-state NMR, tools to quantify the information scrambling dynamics and how it is reflected on the decoherence effects of time-reversal echoes as discussed in Sec. II. We show the implementation of these tools with solid-state NMR quantum simulations.

B. Dynamics (spreading) of quantum information

To set a paradigmatic experiment to spread the local information into a many-body system, one can start from the high-temperature thermal equilibrium state $\rho(0) \approx \left(\mathbb{I} + \frac{\hbar\omega_z}{k_B T} I_z\right)/\mathrm{tr}\{\mathbb{I}\}$, where $I_z = \sum_i I_z^i$ [259]. As the unity operator $\mathbb{I}$ does not contribute to an observable signal, the initial state can be considered as $\rho(0) \propto I_z$ that commutes with the dipolar hamiltonian $\mathcal{H}_{dd}$ [259]. In this equilibrium state, the spins are uncorrelated and thus form an ensemble of local states, which can be thought as the initial local information, similar to the initial position of the spin bearing molecules in the previous section. This state thus represents an ensemble of local pseudo-pure states as described in Sec. II and similar to the ones considered in Ref. [3].

To propagate this local information into the spin network, the system is put out of equilibrium with an evolution operator $U_0(t) = e^{-it\mathcal{H}_0}$, whose Hamiltonian does not commute with the initial state [20, 25]. In spin counting experiments the double-quantum Hamiltonian is typically used [240, 243]

$$\mathcal{H}_0 = -\sum_{i<j} d_{ij}\left[I_x^i I_x^j - I_y^i I_y^j\right]. \tag{20}$$

It is designed by quantum engineering techniques based on dynamical control of the quantum system evolution exploiting average Hamiltonian theory [148]. This Hamiltonian flips simultaneously two spins with the same orientation and thus the z-component of the magnetization m_z changes by $m = \Delta m_z = \pm 2$. The coherence order $m = m_{z,j} - m_{z,i}$ classifies the coherences $|m_{z,i}\rangle\langle m_{z,j}|$ of the density matrix, where $I_z\,|m_{z,i}\rangle = m_{z,i}\,|m_{z,i}\rangle$. The change of coherence order allows probing of the number of correlated spins K as it changes by $\Delta K = \pm 1$ witnessing the information spreading over the system from the initial ensemble of localized states [240, 243, 258]. This cluster size of correlated spins can be associate with an effective volume $\propto \ell^3$, with ℓ the effective "quantum diffusion length" (Fig. 6) [25, 59].

Notice that this picture assumes the many-body system as a closed quantum system, and its non-equilibrium dynamics is determined only by the system Hamiltonian itself. Thus external relaxation mechanisms are neglected, besides the ones effectively produced by the own quantum mechanical evolution of the many-body system driven by the considered Hamiltonians. In a solid-state experiment, the relaxation mechanism that drive the system to thermal equilibrium with the lattice have a characteristic time T_1, that is much longer than the time scale accessible for monitoring the quantum mechanical evolution shown in this section.

The observable in the MQC experiments is the magnetization operator I_z rather than I_x as discussed in Sec. II, thus $M(t) = \mathrm{Tr}\left[I_z\rho(t)\right] \propto \mathrm{Tr}\left[I_z I_z^0(t)\right]$ gives the I_z evolution. The evolved state $\rho(t) \propto I_z^0(t) = U_0(t) I_z U_0^\dagger(t)$ thus contains the dynamics of the information spreading into the spin network. The system state can be expanded in coherence orders as

$$I_z^0(t) = \sum_m \sum_{h(\vec{m},\vec{n})=m} \langle\vec{m}|\, I_z^0(t) |\vec{n}\rangle\, |\vec{m}\rangle\, \langle\vec{n}| = \sum_m I_{z,m}^0(t), \tag{21}$$

where the operator $I_{z,m}^0 = \sum_{h(\vec{m},\vec{n})=m} I_{z,\vec{m}\vec{n}}^0(t) |\vec{m}\rangle\langle\vec{n}|$ contains all the elements of the density operator involving coherences of order m, and $h(\vec{m},\vec{n}) = m$ is the Hamming distance between the states $|\vec{m}\rangle$ and $|\vec{n}\rangle$ [254, 258]. As only the elements with $m = 0$ are observable by the magnetization operator I_z, the magnetization $M(t) \propto \mathrm{Tr}\left[I_{z,0}^0(t)\right]$ decays as a function of time manifesting the information scrambling [59].

C. Time reversal echo as a fidelity of the dynamics of quantum information

MQC are thus useful to probe the quantum information dynamics based on the scrambling of information. They can be used to quantify how sensitive is a quantum evolution to perturbations as a function of the information spreading length ℓ [20, 25, 86, 254]. To assess the sensitivity to perturbations of a controlled quantum dynamics in a many-body system, we can quantify the deviation between the actual driven state $I_z(t) = U_p(t) I_z U_p^\dagger(t)$ and the ideally driven state $I_z^0(t) = U_0(t) I_z U_0^\dagger(t)$, where $U_p(t) = e^{-it\mathcal{H}(p)}$ and $U_0(t) = e^{-it\mathcal{H}_0}$ are the perturbed and ideal control operation, respec-

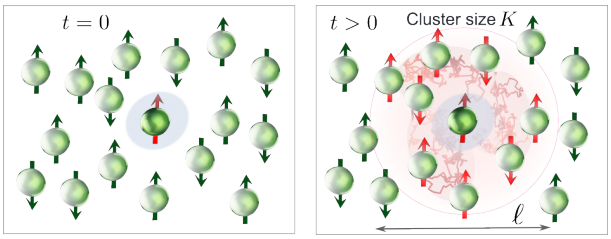

Figure 6. Schematic representation of "quantum spin diffusion" driven quantum mechanical by the many-body system Hamiltonian, without considering external relaxation mechanisms. A spin-coupled network is represented at time $t = 0$ with a local spin excited (red arrow). The spin positions are assumed static. Due to spin-spin coupling interactions, the initial local excitation propagates to the neighbor spins building up highly complex, many-body quantum superpositions. The correlations between the spins due to the quantum superposition are represented by random trajectories connecting the red arrowed spins, defining a cluster size of correlated spins K. The effective "quantum diffusion length" ℓ is associated to an effective volume $\propto \ell^3$ that occupies the cluster size K.

tively. The perturbed Hamiltonian is

$$\mathcal{H}(p) = \mathcal{H}_0 + p\Sigma, \tag{22}$$

with p the strength of the perturbation Hamiltonian Σ.

The instantaneous state fidelity is defined by the inner-product between $I_z(t)$ and $I_z^0(t)$,

$$\mathscr{F}(t) = \mathrm{Tr}\left[I_z(t) I_z^0(t)\right] / \mathrm{Tr}\left(I_z^2\right), \tag{23}$$

where the factor $\mathrm{Tr}(I_z^2)^{-1}$ ensures that $\mathscr{F}(0) = 1$. This fidelity is measured by choosing the observable magnetization I_z equal to the initial condition, then evolving the system with the perturbed evolution operator $U_p(t)$, and then by the inverted Hamiltonian with the unperturbed evolution operator $U_0^\dagger(t)$ [20, 86, 258]. The observable NMR signal after the time reversal echo with a proper normalization is

$$\begin{aligned}\mathscr{F}(t) &= M(t)/M(0) \\ &= \mathrm{Tr}\left(I_z \cdot U_0^\dagger(t) U_p(t) I_z U_p^\dagger(t) U_0(t)\right) / \mathrm{Tr}\left(I_z^2\right),\end{aligned} \tag{24}$$

that is equal to the fidelity after considering cyclic permutations. Figure 7a shows two typical NMR signal decays from solid-state NMR quantum simulations, representing the fidelity for two perturbation strengths.

This fidelity can be written as

$$\mathscr{F}(t) = M(t)/M(0) = e^{-\mathcal{J}(t)}, \tag{25}$$

where the attenuation factor can be described using a perturbative expansion for the echo evolution operator $U_0^\dagger U_p$ [260]. We obtain up to second order on the perturbation strength

$$\begin{aligned}\mathcal{J}(t) &= p^2 \frac{\left[\mathrm{Tr}\left(I_z^2 \Sigma^2(t)\right) - \mathrm{Tr}\left(I_z \Sigma(t) I_z \Sigma(t)\right)\right]}{\mathrm{Tr}\left(I_z^2\right)} + ... \\ &= p^2 \frac{\mathrm{Tr}\left(\left|\left[I_z, \Sigma(t)\right]\right|^2\right)}{\mathrm{Tr}\left(I_z^2\right)} + ..., \\ &= p^2 \int_0^t dt'' \int_0^t dt' K_\Sigma(t', t'') + ...\end{aligned} \tag{26}$$

where $\Sigma(t) = \int_0^t dt' U_0^\dagger(t') \Sigma U_0(t')$ becomes a time dependent perturbation, with the correlation function $K_\Sigma(t', t'') = \frac{\mathrm{Tr}\left(\left[I_z, U_0^\dagger(t') \Sigma U_0(t')\right]\left[I_z, U_0^\dagger(t'') \Sigma U_0(t'')\right]^\dagger\right)}{\mathrm{Tr}(I_z^2)}$. This attenuation factor increases with the perturbation strength p as shown in Fig. 7a,b.

The argument of the double integral is an Out-of-Time-Order Correlation (OTOC) as the operators are not ordered in time [136, 251–253, 261]. If the perturbation Hamiltonian is a dephasing term like $\Sigma = I_z$ [86], we find that the attenuation factor of the fidelity grows as

$$\mathcal{J}(t) = p^2 \int_0^t dt'' \int_0^t dt' \frac{\mathrm{Tr}\left(\left[I_z, I_z^0(t')\right]\left[I_z, I_z^0(t'')\right]^\dagger\right)}{\mathrm{Tr}\left(I_z^2\right)} + ..., \tag{27}$$

with a perturbation correlation function

$$K_0(t', t'') = \frac{\mathrm{Tr}\left(\left[I_z, I_z^0(t')\right]\left[I_z, I_z^0(t'')\right]^\dagger\right)}{\mathrm{Tr}\left(I_z^2\right)} \tag{28}$$

defined by the inner product of the scrambling commutators $\left[I_z, I_z^0(t')\right]\left[I_z, I_z^0(t'')\right]^\dagger$. For $t' = t''$, the OTOC $K_0(t) \equiv K_0(t, t)$ gives the scrambling of information into the system, and thus we expect the fidelity to decay depending on this information scrambling [86, 254].

D. Spin counting by time reversal echo: Out-of-time-order correlations as a measure of information scrambling

As the MQC coherence orders are not observable directly by the spin magnetization, one can recover this spread information and make them again observable, by reversing in time the dynamics driven by the double-quantum Hamiltonian $\mathcal{H}_0$ by changing the sign of $\mathcal{H}_0$ [240]. This leads to a time-reversal echo of the initial magnetization I_z as in Eq. (24) without a perturbation, and the full initial local condition is recovered reflecting the reversible nature of the quantum dynamics [236, 237].

To measure the degree of spreading of the local information into the system, the MQC are encoded by applying a rotation along the z-direction $\phi_z = e^{-i\phi I_z}$. The rotation ϕ_z plays the role of the perturbation to the evolved state $I_z^0(t)$, where the information was encoded. As in

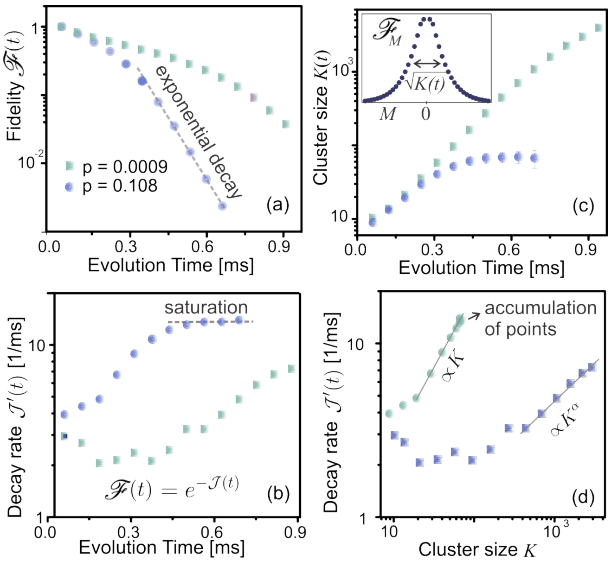

Figure 7. Probing the dynamics of quantum information in many-spin systems with solid-state NMR quantum simulations [86]. (a) Fidelity decay $\mathscr{F}(t) = M(t)/M(0)$ as a function of time for two perturbation strengths. (b) The fidelity decay rate $\mathcal{J}'(t) = \frac{d\mathcal{J}}{dt}(t)$ as a function of time t. (c) Cluster-size of correlated spins and OTOC, $K(t)$ as a function of time, determined from the second moment of the MQC spectrum (inset). The number of correlated spins $K(t)$ defines the "coherence length" on which the dynamics of quantum information are comparable between the ideal and perturbed evolution. (d) The fidelity decay rate $\mathcal{J}'(t)$ as a function of the cluster-size $K(t)$. Notice that the saturation of $\mathcal{J}'(t)$ in panel (b) appears when the cluster size $K(t)$ localizes in (c), which is also evidenced by the accumulation of points in (d). This localized regime occurs when the fidelity decays with an exponential law at times > 0.3ms in (a). The experimental data of the shown quantum simulations were extracted from the spin signals of the hydrogen nuclei of polycrystalline Adamantane on a Bruker Avance III HD 9.4T WB NMR spectrometer with a 1H resonance frequency of $\omega_z = 400.15$ MHz.

Eq. (24), the observable magnetization at the end of the evolution is

$$\mathscr{F}_0(\phi,t) = \frac{1}{\mathrm{Tr}\,(I_z^2)}\mathrm{Tr}\left[I_z\; U_0^\dagger(t)\phi_z U_0(t) I_z U_0^\dagger(t)\phi_z^\dagger U_0(t)\right] = \frac{1}{\mathrm{Tr}\,(I_z^2)}\mathrm{Tr}\left[I_z^0\,(t)\, I_z^{0\dagger}\,(\phi,t)\right], \quad (29)$$

where $U_p(t) = \phi_z U_0(t)$. Each coherence term $|m_{z,i}\rangle\langle m_{z,j}|$ of the evolved state $I_z^0\,(t)$, acquires a phase $m\phi$ due to the rotation perturbation ϕ_z giving

$$\mathscr{F}_0(\phi,t) = \frac{1}{\mathrm{Tr}\,(I_z^2)}\sum_{MM'} e^{iM\phi}\mathrm{Tr}\left[I_{z,M}^0(t) I_{z,M'}^{0\dagger}(t)\right]\delta_{MM'}, \quad (30)$$

where the time reversal fails according to the strength of the perturbation ϕ. The coherence orders $\mathscr{F}_M^0 = \mathrm{Tr}\,(I_z^2)^{-1}\,\mathrm{Tr}\left[I_{z,M}^0(t) I_{z,M}^{0\dagger}(t)\right]$ are obtained by performing a Fourier transform on ϕ [240].

The fidelity of Eq. (29) can be rewritten as

$$\mathscr{F}_0(t,\phi) = \frac{1}{\mathrm{Tr}\,(I_z^2)}\mathrm{Tr}\left[I_z^0\,(t)\,\phi_z I_z^0\,(t)\,\phi_z^\dagger\right] = 1 - \frac{1}{2\mathrm{Tr}\,(I_z^2)}\mathrm{Tr}\left\{\left|\left[I_z^0(t),\phi_z\right]\right|^2\right\}, \quad (31)$$

defining an OTOC function [85, 86, 249, 254, 257]. From a Taylor expansion as a function of ϕ in Eq. (31), we obtain for the attenuation factor

$$\mathcal{J}_0(t,\phi) = \frac{\phi^2}{2\mathrm{Tr}\,(I_z^2)}\mathrm{Tr}\left\{\left|\left[I_z^0(t), I_z\right]\right|^2\right\} = \frac{\phi^2}{2}\sum_M M^2\mathscr{F}_M^0(t), \quad (32)$$

which connects the second moment of the MQC spectrum $\sum_M M^2\mathscr{F}_M^0(t)$ (Fig. 7c) with the OTOC function $K_0(t)$. Therefore, this second moment

$$\sum_M M^2\mathscr{F}_M^0(t) \equiv K_0(t) \quad (33)$$

quantifies the information scrambled into the system by the double-quantum Hamiltonian $\mathcal{H}_0$ [84, 86, 249, 254, 262]. Notice that the attenuation factor of Eq. (32) is equal to the one obtained in Eq. (27), considering that $\phi = pt$ and that the Taylor approximation at short time evolutions gives $K_0(t',t'') \approx K_0(t)$.

This second moment K_0 is typically used in NMR to determine the number of spins where the initial excitation was propagated, generating quantum correlations manifested on the coherence orders [20, 25, 245, 263] –a method called spin counting [240, 244, 246]. To provide a direct connection between the number of correlated spins and the second moment of the MQC spectrum, the propagation model of excitations within the system has to be known. This connection was originally derived by Baum *et. al.* for Gaussian MQC distributions based on a semi-classical picture, where the excitation of the coherence orders evolves as a diffusion processes on the Liouville space [240, 243]. This simple assumption works reasonably well in several solid-state systems [241, 244, 264], but the MQC distribution is not always Gaussian as was observed in several systems [20, 258, 265, 266]. There is no general method to determine the number of correlated spins independently of the system dynamics. A quantitative number of correlated spins is thus typically determined based on dynamics or system-model assumptions [83, 254, 262, 265].

The connection derived in Eq. (33) between the second moment of the MQC spectrum and the OTOC function, allows to derive a more formal definition for the *cluster size of correlated spins* [86, 254]. The second moment K_0 quantifies the degree of non commutation of the evolved state $I_z^0(t)$ and its initial state I_z, with the norm of the commutator $\left|\left[I_z^0(t), I_z\right]\right|$ [86, 248, 249, 262].

The cluster size of correlated spins can be computed by counting the number of active spins during the quantum dynamics, by decomposing the evolved state in Eq. (21) as $I_z^0(t) = \sum_{\vec{u}} c_{\vec{u}}^0(t) P_{\vec{u}}$. Here $c_{\vec{u}}^0(t)$ are time-dependent complex coefficients and $\left\{P_{\vec{u}} = (\sqrt{2})^N \bigotimes_{i=1}^N I_{u_i}^{(1)}\right\}$ is a basis of the composite Hilbert space for N spins 1/2, with the index i labeling the spins, $u_i \in \{0, x, y, z\}$ and $\{I_{u_i}^{(1)}\}$ is the set of single spin operators including the identity operator $I_0^{(1)} \equiv \mathbb{I}$. The second moment is thus [254]

$$K_0(t) \sim \sum_{\vec{u}} \left|c_{\vec{u}}^0(t)\right|^2 L(\vec{u}), \tag{34}$$

where the magnitude $L(\vec{u})$ quantifies the number of *active spins* associated with the coherence transfer process $\langle\vec{n}|P_{\vec{u}}|\vec{m}\rangle$ [267, 268] based on quantifying the number of non-identity operators and non-I_z operators in $P_{\vec{u}}$.

The second moment K_0 of the MQC spectrum is thus the average number of active spins in the state $I_z^0(t)$, weighted by the dynamical coefficients $\left|c_{\vec{u}}^0(t)\right|^2$ determined by the spreading of quantum information through the quantum evolution. This thus provides an interpretation for the information scrambling in spin systems based on a "diffusion coherent length" associated with the number of active spins. As $L(\vec{u})$ defines a Hamming distance, Eq. (34) provides a way of quantifying a correlation length as an average Hamming distance that determines the quantum information spreading quantified by the OTOC function of Eq. (33) [254].

E. Fidelity of the spatial spreading of quantum information based on a generalized MQC spectrum and OTOC

To assess the sensitivity to perturbations of the scrambling dynamics of information, similarly to the encoding of conventional MQC in Sec. IV D, we apply the rotation operation $\phi_z = e^{i\phi I_z}$ between the perturbed (forward) evolution $U_p(t)$ and ideal (backward) evolution $U_0^\dagger(t)$ (used in Sec. IV C) [20, 258]. The fidelities of Eqs. (24) and (29) now becomes

$$\begin{aligned}\mathscr{F}_\phi(t) &= \mathrm{Tr}\left(U_0^\dagger(t)\phi_z U_p(t) I_z U_p^\dagger(t)\phi_z^\dagger U_0(t)\cdot I_z\right)/\mathrm{Tr}\left(I_z^2\right)\\ &= \mathrm{Tr}\left[I_z(t)\phi_z^\dagger I_z^0(t)\phi_z\right]/\mathrm{Tr}\left(I_z^2\right)\\ &= \textstyle\sum_m e^{i\phi m}\mathscr{F}_m(t)/\mathrm{Tr}\left(I_z^2\right),\end{aligned} \tag{35}$$

where the last row of the equation defines a generalized MQC spectrum. It is defined by the partial fidelities of different coherence orders m, determined by the MQC inner-products [20, 25, 86]

$$\mathscr{F}_m(t) = \mathrm{Tr}\left[I_{z,m}(t) I_{z,m}^0(t)\right]/\mathrm{Tr}\left(I_z^2\right). \tag{36}$$

This generalized MQC spectrum quantifies the deviation of the density operator elements of the perturbed evolution for a given m. It is equal to the conventional MQC spectrum if the perturbation strength $p = 0$.

The fidelity $\mathscr{F}_\phi(t)$ is now related with a more general OTOC that quantifies the deviation of the information dynamics induced by the perturbed Hamiltonian $\mathcal{H}(p)$ with respect to the one that is driven by the ideal Hamiltonian $\mathcal{H}_0$ [86, 254]

$$\begin{aligned}\mathscr{F}_\phi(t) &= \frac{\mathrm{Tr}\left[I_z^0(t)\,\phi_z I_z^\dagger(t)\,\phi_z^\dagger\right]}{\mathrm{Tr}\left(I_z^2\right)}\\ &= \frac{\mathrm{Tr}\left[I_z^0(t) I_z^\dagger(t)\right]}{\mathrm{Tr}\left(I_z^2\right)}\left(1 - \frac{\mathrm{Tr}\left(\left[\phi_z, I_z^0(t)\right]\left[\phi_z, I_z(t)\right]^\dagger\right)}{2\mathrm{Tr}\left[I_z^0(t) I_z^\dagger(t)\right]}\right).\end{aligned} \tag{37}$$

Here the term $\frac{1}{\mathrm{Tr}(I_z^2)}\mathrm{Tr}\left[I_z^0(t) I_z^\dagger(t)\right]$ is the overall fidelity of Eq. (23), and the term in the parenthesis contains a more general OTO commutator $\mathrm{Tr}\left(I_z^2\right)^{-1}\mathrm{Tr}\left(\left[\phi_z, I_z^0(t)\right]\left[\phi_z, I_z(t)\right]^\dagger\right)$ than the one found in Eq. (31).

This OTOC quantifies the deviation of the perturbed evolution by the overlap of the commutators $\left[\phi_z, I_z^0(t)\right]$ and $\left[\phi_z, I_z(t)\right]$ via the inner-product [86, 254]. Again after a Taylor expansion as a function of ϕ, we obtain that the attenuation factor has a term given by the second moment of the generalized MQC spectrum $\mathscr{F}_m(t)$

$$K(t) = \frac{\sum_m m^2 \mathscr{F}_m(t)}{\sum_m \mathscr{F}_m(t)} = \frac{\mathrm{Tr}\left(\left[I_z(t), I_z\right]^\dagger\left[I_z^0(t), I_z\right]\right)}{\mathrm{Tr}\left[I_z^0(t) I_z^\dagger(t)\right]}. \tag{38}$$

This second moment of the generalized MQC spectrum thus provides an OTOC, that gives the degree of non-commutation shared by the evolved states $I_z^0(t)$ and $I_z(t)$ with respect to I_z based on the inner-product between the commutators $[I_z(t), I_z]$ and $[I_z^0(t), I_z]$ [86, 254]. Figure 7c shows the growth of this second moment as a function of time for two perturbation strengths from solid-state NMR quantum simulations.

Determining the active spins during the dynamics as in Eq. (34), we obtain that the second moment is [254]

$$K(t) \simeq \frac{1}{\sum_{\vec{u}} c_{\vec{u}}^0(t) c_{\vec{u}}^{p*}(t)} \sum_{\vec{u}} c_{\vec{u}}^0(t) c_{\vec{u}}^{p*}(t) L(\vec{u}), \tag{39}$$

where now $c_{\vec{u}}^p(t)$ are time-dependent complex coefficients of the perturbed quantum evolution. This expression now gives the average number of active spins that are shared by the ideal and perturbed quantum information dynamics. This result demonstrates that the OTOC of Eq. (38) is an average Hamming distance based on the active spins, weighted by the product between the ideal and perturbed evolution coefficients $c_{\vec{u}}^0(t) c_{\vec{u}}^{p*}(t)$.

The key implication of this result is that the second moment of the generalized MQC spectrum, related with the generalized OTOC of Eq. (38), defines a "coherent diffusion length" of the scrambling dynamics of information between the ideal and perturbed evolution. Based on the MQC fidelity $\mathscr{F}_m(t)$, it quantifies the scrambling of

information by the spin-spin interactions of $\mathcal{H}_0$ that survived the perturbation effects, and thus it shrinks with increasing the perturbation p (Fig. 7c) [20, 25, 86]. Alternatively, the second moment $K(t)$ thus quantifies how comparable are the perturbed and unperturbed quantum information dynamics as a function of the multiple quantum coherence order m. Notice that the non-equilibrium many-body dynamics observed with these techniques thus reflect the coherent dynamics generated by the engineered Hamiltonians. This is quantified by the signal that survives the decoherence effect induced by other degrees of freedom that were not considered in the described Hamiltonians [25].

F. Fidelity of quantum information dynamics as a function of the coherent diffusion length

Based on a second-order approximation analysis in Sec. IV C, we found that the fidelity between the ideal and perturbed dynamics decays with an attenuation factor that depends on the OTOC function $K_0(t', t'')$. This OTOC is defined by the inner product of the scrambling commutators $\left[I_z, I_z^0(t')\right]\left[I_z, I_z^0(t'')\right]^\dagger$. For $t' = t''$, the OTOC gives the second moment of the MQC spectrum $K_0(t)$ that provides the average number of active spins in the dynamics.

In analogy with the molecular diffusion problem of Sec. III, where the fluctuations of the environment are described by a classical diffusion process, here the decoherence decay of the time reversal echoes depends on the quantum scrambling dynamics of the initial information stored on I_z. The average number of active spins $K_0(t)$ plays the role of the root mean squared displacement in the molecular diffusion $\langle \Delta r(t) \Delta r(t) \rangle$. The OTOC function $K_0(t', t'')$ in the attenuation factor of Eq. (27), thus plays the role of the displacement correlation function $\langle \Delta r(t') \Delta r(t'') \rangle$.

The experimental results so far have demonstrated that the fidelity of the quantum information dynamics decays with a power law $\mathcal{J}'(t) \propto (K(t))^\alpha$ as a function of the second moment of the generalized MQC spectrum (Fig. 7d) [86, 254]. The exponent α depends on the perturbation strength. Although a non-perturbative analysis needs to be performed to contrast with a theoretical prediction, this demonstrates that the fragility of the quantum evolution depends on the "coherent diffusion length" determined by the average number of active spins $K(t)$, which quantifies the scrambling of the quantum information.

Notice that for large perturbations, the effective number of active spin where the information propagated reliably –quantified by the generalized OTOC $K(t)$– localizes, while for low perturbations it propagates indefinitely on the observed time scales (Fig. 7) [20, 25, 86]. This shows that perturbations larger than a given threshold set a bound to the coherent length where information can be propagated reliably. The decoherence scaling law is linear with $K(t)$, i.e. $\mathcal{J}'(t) \propto K(t)$, when the localization behavior is observed (Fig. 7d). A linear dependence for this decay rate is predicted from the second-order approximation of Eq. (27). Assuming that at this perturbation regime, the correlation function decays fast with a characteristic time τ_c, we find that $\mathcal{J}(t) \approx p^2 \int_0^t dt'' \int_0^t dt' K_0(t', t'') \approx p^2 \tau_c \int_0^t dt' K_0(t)$ and thus the decoherence rate is $\mathcal{J}'(t) \propto K_0(t)$.

Summary: Tools for assessing the reliability of controlling the dynamics of quantum information

The tools introduced in this section, provide a paradigmatic strategy to characterize the dynamics of quantum information, based on the spreading of a local state into a many-body system. The introduction of controlled perturbations plays the role of control imperfections, thus setting an approach to studying the robustness of control operations during the propagation of quantum information. We show tools combining NMR techniques and quantum information metrics that quantify the sensitivity to perturbations of the information propagation dynamics. Remarkably, they characterize the control operation's sensitivity based on a spatial assessment of how reliably the information was propagated. The generalized fidelity of the control operation is based on the coherent length of the controlled information, rather than only providing a global fidelity. All these combinations of tools provide a framework for benchmarking quantum hardware and control technologies to achieve robust and reliable control strategies for developing quantum technologies.

V. SELECTIVE PROBING OF COUPLING STRENGTHS: MOLECULAR AND SPIN NETWORK CHARACTERIZATION

In this Section, we present a control strategy to probe the sensor-environment coupling g, when the full spectral density $S(\omega)$ is *unknown* or too complex to be fully estimated. We here show that the best precision estimation can still be achieved with a rough knowledge of the overall width of the environment spectral density ($\approx \tau_c^{-1}$). To achieve this precision bound, we apply stroboscopic QND measurements conforming to a QZE regime to filter out the unknown details of the environment. We exemplify the usefulness of this, with two experimental setups.

A. Quantum Zeno estimation for selective sensing

The ultimate error bound in the estimation of g is attained in the regime where $\mathcal{J} \propto g^2$ ($x_E^\alpha = g^2$ being $\alpha = 2$, in Eq. (10) of Sec. II D). Since the coupling strength is $g^2 = \int d\omega S(\omega)$, this regime is achieved when the filter function $F_t(\omega) = F_t$ is flat in the main domain of $S(\omega)$

(see Eq. (6), and violet filter in Fig. 1c) [137]. Then, the attenuation factor $\mathcal{J} = F_t g^2$ need also to fulfill the condition $\mathcal{J} = \mathcal{J}_0$. A freely evolving qubit-sensor produces a flat filter $F_t \propto t^2$ in the main domain of $S(\omega)$ only if $t \ll \tau_c$, leading to $\mathcal{J} \propto t^2 g^2$. But in general, this short time is not enough to attain $\mathcal{J}_0$, and dynamical control is needed.

A flat filter at times longer than the environment correlation time τ_c is obtained via stroboscopic QND measurements on the qubit-probe in the basis of $|\pm\rangle$. Performing repeated cycles of free evolution interlaced with QND measurements at a rate larger than τ_c^{-1}, conform the quantum Zeno regime (see Fig. 1) [137, 151]. The filter function then describes a spectral broadening far beyond the width of $S(\omega)$ (Fig. 1c). As the free evolution is thus interlaced by these stroboscopic projections that resets the initial state of the qubit-probe, its attenuation factor is given by a free evolution one during the stroboscopic time t/N, multiplied by the number of projections N, i.e. [43, 53, 137, 177]

$$\mathcal{J}(g,t) = \frac{g^2 t^2}{2N}, \tag{40}$$

where the time interval between the QND measurements $\frac{t}{N} \ll \tau_c$ for a total control time t. Thus, the ultimate error bound of Eq. (10) is attained, by adjusting the total control time to $t = \sqrt{2N\mathcal{J}_0}/g$ provided that $N \gg \frac{2\mathcal{J}_0}{g^2\tau_c^2}$ [137].

The advantage of attaining this Zeno regime is that it requires only to satisfy the condition $\frac{t}{N} \ll \tau_c$ for the time interval between measurements, rather than the total evolution time t. This quantum control tool allows extending the probing time to the optimal estimation time for attaining the ultimate precision limit [137]. The outcomes of the QND measurements do not need to be read out, as the measurements are only used to steer the qubit-probe evolution. Thus QND measurements can be *emulated* by dephasing induced by noise on the qubit probe thus effectively projecting its quantum state to the suitable basis [50, 53, 177]. This is typically done by induced dephasing produced by magnetic field gradients [50, 53, 152], T_2 relaxation [78] or stochastic interactions [163, 269, 270].

We now show two examples where QND measurements in the QZE regime are used to determine the coupling strengths of complex spin-networks [53]: An illustration of the method from experimental implementations in liquid state NMR, and an experimental proposal with NVc in diamond as a qubit-probe, to attain the precision estimation bound of coupling strengths with the environment by implementing an online-learning protocol.

B. Molecular coupling inference from spin-coupling network topologies

In chemistry and in quantum technologies, one is interested to characterize the entire coupling network topology of the spins/qubits [53, 75, 163, 271–273]. However, spin-coupling network topologies in many-body system are in general very complex, and the inference from their coherent evolution is thus also very complex. This complexity for determining the entire coupling-network structure makes the multi-parameter estimation very difficult and unpractical in several situations [53, 163]. The QZE control strategy introduced here thus was implemented to simplify these complex many-spin dynamics that depend on several parameters, by implementing projected evolutions [50, 53]. The QND measurements were experimentally implemented by applying repetitive random magnetic field gradients [50, 53] or stochastic processes [78, 163, 269, 270] to the qubit-probe. We here thus show this facilitation for the estimation of the couplings strengths by the implementation of the QZE estimation protocol.

We consider a Hamiltonian with an isotropic (Heisenberg) interaction between the spins as it is typically found in liquid state NMR [53, 75, 271–273]. The Hamiltonian is

$$\mathcal{H} = \sum_i \omega_i^z I_i^z + \sum_{i<j} g_{ij} \mathbf{I}_i \cdot \mathbf{I}_j, \tag{41}$$

where i indexes the different spins, ω_i^z are the chemical shifts, and g_{ij} are the coupling strengths between spins i and j. We need to attain the QZE regime, where the evolution time is shorter that the correlation time of the environment of a given spin of the molecule, i.e. a time $t \ll g_{ij}^{-1}, \left(\omega_i^z - \omega_j^z\right)^{-1}$. Within this regime, we can thus approximate the evolution operator by using the first order Trotter-Suzuki expansion that leads to

$$U(t) = \mathrm{e}^{-iHt/\hbar} \approx \prod_i \mathrm{e}^{-it\omega_i^z I_i^z} \prod_{i<j} \mathrm{e}^{-itg_{ij}\mathbf{I}_i\cdot\mathbf{I}_j}. \tag{42}$$

We consider an initial condition where a given spin is excite/polarized and the remaining spins unpolarized $\rho(0) = \mathbf{1} + \delta p I_i^z$, in a kind of pseudo-pure state [3]. Thus, the quantum evolution of its magnetization is determined by the evolution of the operator I_i^z. At short times $t \ll g_{ij}^{-1}, \left(\omega_i^z - \omega_j^z\right)^{-1}$, its evolution is given by

$$I_i^z \to \sum_{j\neq i} \left[I_i^z \left(1 - \frac{g_{ij}^2 t^2}{8}\right) + I_j^z \frac{g_{ij}^2 t^2}{8} \right] + \mathcal{O}, \tag{43}$$

where the term $\mathcal{O}$ includes the higher Trotter-Suzuki expansion orders in time, and non-observable terms when monitoring the evolution of the I_i^z operator steered by the non-demolition measurements [53]. At this short time scale, the dynamics when observed from the initially excited spin gives the magnetization $M(t) = \mathrm{Tr}\left[\rho(t) I_i^z\right]$. Its evolution can be mapped to the one obtained for a central spin i that is homogeneously coupled to the remaining spins j, with an effective interaction $g = \sqrt{\frac{1}{N}\sum_j g_{ij}^2}$ with N the number of neighbor spins [274]. The spins j are thus considered as the environment here, and at this

QZE regime the details of the interactions between them are invisible, thus allowing to estimate the effective interaction strength g of the spin-probe spins with the environmental spins j. This simplifies significantly the complex dynamics of a large molecule as was demonstrated in Ref. [53]. Then by optimizing the total evolution time to $t = \sqrt{2N\mathcal{J}_0}/g$ along this projected evolution, this coupling strength can be efficiently estimated by attaining its ultimate precision bound based on Eq. (9).

C. Real-time adaptive learning of coupling interactions with a NV center quantum probe

Attaining the ultimate precision limit requires a previous knowledge of the parameters to be estimated, as the optimization protocol depends explicitly on the unknown parameter x_E [137]. Thus, for example, the predicted optimal time $t = \sqrt{2N\mathcal{J}_0}/g$ for this QZE estimation protocol to estimate the coupling depends on g. To circumvent this optimization procedure one can monitor and control the probe using an efficient real-time adaptive estimation protocol [137, 275–277]. Figure 8 illustrates such a protocol and shows how it can attain the predicted ultimate precision bound, Eq. (10), when the qubit-probe is optimally controlled.

The protocol is general to estimate any parameter, and it is based on an online experimental learning design based on Bayesian statistics to maximize an information gain The real-time adaptive protocol consists of *(i)* first assume a probability distribution $p(x_E)$ for the unknown parameter x_E based on some prior knowledge. *(ii)* Then determine the optimal control of the qubit-probe based on maximizing *the information gain* about the parameter x_E, which depends on probability distribution $p(x_E)$ and a *likelihood function* $p(d|x_E, t)$ of obtaining the possible outcome data of the qubit measurement $d = \{+, -\}$ in the basis $|\pm\rangle$. In our QZE protocol, the optimal control is based on finding the best time t_m to perform a measurement. *(iii)* We then perform the qubit-probe measurements of its state, at the predicted optimal control time t_m. According to the outcome data d from the measurements, we update the knowledge of x_E using the Bayes Rule

$$p^{new}(x_E) \equiv p(x_E|d, t_m) = \frac{p(d|x_E, t_m)\, p(x_E)}{p(d|t_m)}, \qquad (44)$$

where $p(d|t)$ is a normalization factor for integration over x_E. The estimation of the unknown parameter x_E is an iterative process that repeats these three-stages $\mathcal{N}_m$ times, where $\mathcal{N}_m$ stands for the number of measurements. The knowledge of x_E thus improves iteratively when optimal control is used, and its probability distribution $p(x_E)$ converges to a narrow peak around its true value x_E^{true} (Fig. 8b).

Figure 8 shows numerical simulations based on experimental data of the intrinsic environmental characteristics of a NVc spin-probe [278]. The coupling strength g is here related the coupling interaction with the NVc environment. We simulate the implementation of the QZE protocol compared with free evolution (further details can be found in Ref. [137]). Projective measurements may be emulated by a brief (stroboscopic) induced dephasing [50, 53] of the NVc coherence based on radiative decay to the electronic ground state, which is longitudinally spin-conserving [279] and effectively collapses the wave function. For the simulations, we assume the projective measurements are perfect and instantaneous.

Figures 8d,e compare the predicted optimal time by the

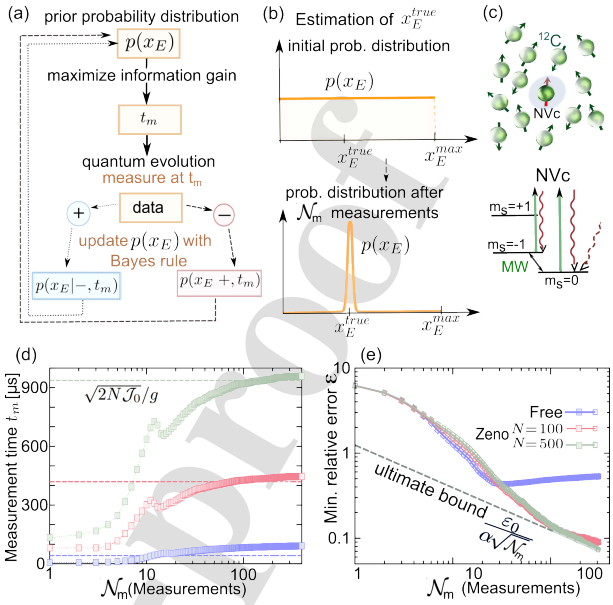

Figure 8. Real-time adaptive estimation protocol. (a) Scheme of the estimation protocol of the parameter x_E, based on a Bayesian estimator and an online experimental learning design that maximizes the information gain, so as to find the best measurement time. (b) Convergence of the probability distribution $p(x_E)$ under optimal control of the spin-probe. Starting from an initial prior distribution, the protocol converges to a narrow one with a peak centered at x_E^{true}, after $\mathcal{N}_m$ measurements (one per loop in this algorithm). (c) Nitrogen Vacancy Center (NVc) as spin-sensor of a ^{12}C diamond sample [278]. The environmental spectral density is a Lorentzian function with $\tau_C = 10\mu$m and a coupling $g = 0.03$MHz. In this setup, projective measurements result from applying MW $\pi/2$ pulses on the $0 \leftrightarrow -1$ transition and a laser-induced relaxation (green arrows) between the ground and exited electronic states that preserve the spin (solid curly arrows). At the end of the sequence, the readout is completed by measuring the laser-induced fluorescence intensity (d) Convergence to the optimal time t for estimating $x_E = g$ as a function of $\mathcal{N}_m$; and (e) the corresponding minimal relative error in the estimation of g, measuring at the estimated time t_m at each step $\mathcal{N}_m$. Here, free evolution and Zeno control with $N = 100, 500$ are averaged over 600 realizations. The ultimate bound ($\frac{\varepsilon_0}{2\sqrt{\mathcal{N}_m}}$ dashed line, $\alpha = 2$) is only attained by Zeno control when $t_m \approx \sqrt{2N\mathcal{J}_0}/g$ consistently with our theoretical predictions.

real-time learning estimation protocol and the attained minimum relative error as a function of the iteration step $\mathcal{N}_m$. The results are shown for the qubit-probe measurements after free evolution and with $N = 100$ and $N = 500$ stroboscopic measurements during the predicted optimal time t_m. Clearly, the free evolution estimation protocol does not converge to the ultimate precision bound due to the lack of knowledge of the full spectral density of the environment. However, the QZE protocol reduces the minimum relative error of the estimation without assuming knowledge of the full spectral density, and with 500 projective measurements, it converges to the ultimate precision bound. The optimal stroboscopic times between the projective measurements are found to be in this case $\frac{t}{N} \approx 1.9\mu s$, which is consistent with the predicted optimal time by the ultimate precision bound of Eq. (10).
Thus these results demonstrate that the ultimate precision bound for the coupling strength with the environment can be attained without prior knowledge of the full spectral density. Moreover, they also show that real-time adaptive learning protocols can be implemented to circumvent the requirement of prior knowledge of the value of the parameter to be estimated.

Summary: Selective and iterative online learning inferences

In this Section, we show how implementing incoherent control to attain the QZE regime, allows the selective inference of parameters. This strategy simplifies the qubit-probe dynamics and the inference procedure by filtering out the complexity of the full environment. More importantly, it also attains the ultimate estimation precision bounds in the standard quantum limit. With this paradigmatic example, we highlighted the loophole of efficient parameter estimation by dynamical control: it requires prior knowledge of the parameter value. In cases where no prior knowledge exists, real-time adaptive learning can be implemented to the inference protocol, that iteratively converge to the optimal control and estimation precision bounds. Although these inference protocols are exemplified estimating coupling strengths, the approach is general and adaptable to infer other parameters. The selective inference strategy of a relevant parameter may also be a paradigmatic approach for finding the fastest possible way of attaining information, as it only focuses on the relevant one.

VI. CONCLUSIONS AND PERSPECTIVES

We provide a brief overview of some tools that we are contributing to develop from Latin America and positioning them in the context of synergistically merging the fields of nuclear magnetic resonance and quantum information sciences and technologies. We introduce these tools in the context of the state-of-the-art in developing methods for quantum sensing of physical, chemical, and biological processes. The main concepts for decoherence and relaxation control based on sequences of electromagnetic field pulses are described. In terms of decoupling techniques in magnetic resonance, these strategies are typically used to extend the lifetime of quantum states or dynamics. Rather than extending their characteristic times, we focus on designing decoupling sequences to exploit decoherence and relaxation mechanisms as key information resources.

We introduce the main concepts for designing quantum control to extract efficiently and/or selectively the relevant information from the decay time of spin signals. Quantum control thus rather than reducing decoherence, steers it to infer spectral and time correlation properties on the environment of the quantum sensors –the spins-1/2. We show how key concepts that merge quantum dynamical control and information estimation tools with magnetic resonance fields, can be applied to specific goals such as characterizing biological tissue microstructure with diffusion weighting imaging, monitoring the dynamics of quantum information and its connections with out-of-equilibrium many-body physics, and molecular characterization through selective estimations of spin-spin couplings.

Although the methods and strategies are illustrated with these specific examples spanning a variety of fields, the concepts for designing suitable control to infer the information are general. Implementations of the presented approaches can thus be adapted to different experimental setups and/or applications.

The importance of extracting information in the fastest time possible is evidenced by the need for deep biological tissue imaging at the microscopic and nanoscale. Invasive or surface imaging technologies might attain these scales, however the strength of NMR is that potentially can achieve those scales in deep tissue, non-invasively. Highly relevant information on biological functions and pathologies within a pixel of an MRI image is typically very large and complex, as the typical spatial scale of the MRI resolution and the biologically relevant scales differ by orders of magnitude. We show how suitable quantum control of the information stored on nuclear spins, that self-diffuse within the tissue microstructure, can extract microscopic features from the restriction boundaries that the molecules feel. Quantum estimation tools provide the ultimate precision limits for estimating tissue microstructure parameters, as well as metrics for determining the best control sequence design to achieve them. These findings also allow for the assessment of the feasibility of observing microstructure features quantitatively.

As a step towards extracting information independently of model assumptions that represent the quantum-probe environment, we show how selectively observe specific microstructure sizes. We introduce examples on how suitably designed pulse sequences may help develop tools for scanning microstructure size distributions without as-

suming a model a priori. The combination of selective and efficient extraction of information from tissue microstructure may help pave the way to find quantitative diagnostic tools, that can be implemented in practical acquisition times compatible with in-vivo imaging, where the relevant information needs to be extracted fast.

Through experimental observation and exploration, methods currently used for extracting tissue microstructure features might probably be implemented in optimal ways that are consistent with the prediction derived from the presented quantum estimation tools. As biological systems are very complex, still it is very important to complement those findings and explorations with fundamental concepts and derivations that provide the estimation limits. This combination of approaches can help evaluate the self-consistency of model assumptions, quantitative estimations, and mathematical representations, as validating tissue microstructure features is extremely difficult in non-invasive ways. Even with the implementation of invasive observations, there are no clear mechanisms to validate quantitative methods without distorting the natural tissue. We thus find that self-consistent estimation protocols based on non-invasive observation contrasted with fundamental predictions and evaluations might help to reconstruct tissue microstructure information without prior knowledge.

Another important application related to extracting information from complex systems with a large number of degrees of freedom is the monitoring of the dynamics of quantum information. We show how starting from localized states, its propagation can be probed from decoherence manifested on time reversal echoes. Here a "quantum diffusion mechanism" driven by quantum mechanical evolutions induces fluctuation in the spins states inducing decoherence when a perturbation is introduced to the control Hamiltonians. Several NMR studies starting in the '80s explored the complex spin dynamics of many-body systems. Probably due to the challenging nature of understanding these many-body systems, in particular when they are out-of-equilibrium, a gap of years exists without active research on the topic, until quantum information processing trigger again the interest.

It is still not fully understood how a local excitation "diffuses" quantum mechanically in a complex spin network and might eventually thermalize without an external reservoir. The developments and new motivations within quantum information processing and simulations fields have thus attracted new attention to these outstanding problems. New techniques and approaches were introduced that can now be applied to study these complex dynamics. Considering quantum systems as quantum simulators have changed significantly the strategies to push forward the frontiers of our knowledge of many-body systems out of equilibrium. This approach allows adapting a set of established, but more importantly, robust tools developed in NMR and condensed matter physics, as building blocks to generate new types of engineering to monitor the non-equilibrium dynamics. This combination of approaches is now being exploited to understand the interplay of different types of interactions and the dynamical behavior of spin systems.

Out-of-Time-Order Correlations (OTOCs) triggered a broad interest in diverse fields of physics. They introduced new mechanisms and interpretations for understanding the dynamics of quantum information in large and complex quantum systems. OTOCs are a quantitative tool to measure the scrambling of quantum information starting from a local excitation into the system's degrees of freedom. We show how multiple quantum coherences developed within NMR are an important proxy to measure the OTOCs, and how they are both connected to monitor the evolution of the number of active spins that are correlated by the quantum information distributed over the spin network. We illustrate how a suitable design of time reversal echo sequences can provide tools for characterizing via decoherence effects the control of many-body systems out-of-equilibrium with realistic operations that intrinsically contain imperfections. These tools can quantify how fragile and sensitive is a controlled dynamics to the control imperfections. These tools thus provide protocols for achieving robust quantum systems and control strategies for designing and deploying quantum technologies.

Last but not least, we show an application of merging quantum control and information tools for the selective inference of parameters, that might also be a key to developing novel technologies for extracting information in the fastest time possible. As full knowledge of a system will probably remain impossible for several practical applications, filtering relevant information is a key paradigm for diagnosing systems and processes. We thus show particular examples of how suitable quantum control, filters out a large set of degrees of freedom, to only be sensitive to specific parameters. We exemplify this concept with the specific example of inferring spin-spin couplings, useful for molecular characterization and Hamiltonian learning, up to their ultimate precision limits. We used also this example, to show how real-time adaptive learning can also be incorporated for the designing of optimal control strategies, and to achieve iteratively the ultimate precision limits of the information.

As a concluding remark, NMR has shown to be a leading quantum technology to exploit quantum dynamical control for highly relevant quantum sensing applications. They span from molecular characterization to imaging applications, exploiting decoherence mechanisms, multiple quantum coherences, many-spin quantum correlations, and quantum imaging modalities. NMR is a very versatile technique for dynamically control quantum-states and is well-developed for sensing applications. One of the strengths of NMR is its non-invasive nature, which makes the technique very suitable for in-vivo studies of biological systems such as animals and humans. Thus exploiting quantum control and estimation tools for designing novel diagnostic methods is an area where NMR plays an important role, as alternative quantum tech-

nologies will face very difficult challenges to achieve non-invasive strategies.

ACKNOWLEDGMENTS

This work was supported by CNEA; CONICET; ANPCyT-FONCyT PICT-2017-3156, PICT-2017-3699, PICT-2018-4333, PICT-2021-GRF-TI-00134, PICT-2021-I-A-00070; PIP-CONICET (11220170100486CO); UNCUYO SIIP Tipo I 2019-C028, 2022-C002, 2022-C030; Instituto Balseiro; A collaboration program from MINCyT (Argentina) and MAECI (Italy) and Erasmus+ Higher Education program from the European Commision between the CIMEC (University of Trento) and the Instituto Balseiro (Universidad Nacional de Cuyo).

[1] N. A. Gershenfeld and I. L. Chuang, Science **275**, 350 (1997).
[2] D. G. Cory, A. F. Fahmy, and T. F. Havel, Proceedings of the National Academy of Sciences of the United States of America **94**, 1634 (1997).
[3] E. Knill and R. Laflamme, Phys. Rev. Lett. **81**, 5672 (1998).
[4] R. Laflamme, D. G. Cory, C. Negrevergne, and L. Viola, arXiv preprint quant-ph/0110029 (2001).
[5] C. Ramanathan, N. Boulant, Z. Chen, D. G. Cory, I. Chuang, and M. Steffen, Quantum Information Processing **3**, 15 (2004).
[6] L. M. K. Vandersypen and I. L. Chuang, Rev. Mod. Phys. **76**, 1037 (2005), copyright (C) 2009 The American Physical Society; Please report any problems to prola@aps.org.
[7] J. D. Bulnes, F. A. Bonk, R. S. Sarthour, E. R. d. Azevedo, J. C. C. Freitas, T. J. Bonagamba, and I. S. Oliveira, Braz. J. Phys. **35**, 617 (2005).
[8] J. Stolze and D. Suter, *Quantum computing: a short course from theory to experiment* (John Wiley & Sons, 2008).
[9] I. Oliveira, R. Sarthour Jr, T. Bonagamba, E. Azevedo, and J. Freitas, *NMR quantum information processing* (Elsevier, 2011).
[10] D. Lu, A. Brodutch, J. Park, H. Katiyar, T. Jochym-O'Connor, and R. Laflamme, Electron Spin Resonance (ESR) Based Quantum Computing , 193 (2016).
[11] L.-M. Duan, E. Demler, and M. D. Lukin, Phys. Rev. Lett. **91**, 090402 (2003).
[12] W. S. Bakr, J. I. Gillen, A. Peng, S. Fölling, and M. Greiner, Nature **462**, 74 (2009).
[13] S. Diehl, A. Micheli, A. Kantian, B. Kraus, H. P. Büchler, and P. Zoller, Nat. Phys. **4**, 878 (2008).
[14] P. Jurcevic, B. P. Lanyon, P. Hauke, C. Hempel, P. Zoller, R. Blatt, and C. F. Roos, Nature **511**, 202 (2014).
[15] E. A. Martinez, C. A. Muschik, P. Schindler, D. Nigg, A. Erhard, M. Heyl, P. Hauke, M. Dalmonte, T. Monz, P. Zoller, and R. Blatt, Nature **534**, 516 (2016).
[16] K. A. Landsman, C. Figgatt, T. Schuster, N. M. Linke, B. Yoshida, N. Y. Yao, and C. Monroe, Nature **567**, 61 (2019).
[17] M. Saffman, T. G. Walker, and K. Molmer, Rev. Mod. Phys. **82**, 2313 (2010).
[18] J. Schachenmayer, B. P. Lanyon, C. F. Roos, and A. J. Daley, Phys. Rev. X **3**, 031015 (2013).
[19] B. Yan, S. A. Moses, B. Gadway, J. P. Covey, K. R. A. Hazzard, A. M. Rey, D. S. Jin, and J. Ye, Nature **501**, 521 (2013).
[20] G. A. Álvarez and D. Suter, Phys. Rev. Lett. **104**, 230403 (2010).
[21] G. A. Álvarez and D. Suter, Phys. Rev. Lett. **107**, 230501 (2011).
[22] A. M. Souza, G. A. Álvarez, and D. Suter, Phys. Rev. Lett. **106**, 240501 (2011).
[23] P. E. S. Smith, G. Bensky, G. A. Álvarez, G. Kurizki, and L. Frydman, Proc. Natl. Acad. Sci. U. S. A. **109**, 5958 (2012).
[24] G. A. Álvarez, N. Shemesh, and L. Frydman, Phys. Rev. Lett. **111**, 080404 (2013).
[25] G. A. Álvarez, D. Suter, and R. Kaiser, Science **349**, 846 (2015).
[26] R. Fischer, C. O. Bretschneider, P. London, D. Budker, D. Gershoni, and L. Frydman, Phys. Rev. Lett. **111**, 057601 (2013).
[27] T. Staudacher, F. Shi, S. Pezzagna, J. Meijer, J. Du, C. A. Meriles, F. Reinhard, and J. Wrachtrup, Science **339**, 561 (2013).
[28] G. Waldherr, Y. Wang, S. Zaiser, M. Jamali, T. Schulte-Herbrüggen, H. Abe, T. Ohshima, J. Isoya, J. F. Du, P. Neumann, and J. Wrachtrup, Nature **506**, 204 (2014).
[29] G. A. Álvarez, C. O. Bretschneider, R. Fischer, P. London, H. Kanda, S. Onoda, J. Isoya, D. Gershoni, and L. Frydman, Nat. Commun. **6**, 8456 (2015).
[30] T. Staudacher, N. Raatz, S. Pezzagna, J. Meijer, F. Reinhard, C. A. Meriles, and J. Wrachtrup, Nat. Commun. **6**, 8527 (2015).
[31] P. R. Zangara, S. Dhomkar, A. Ajoy, K. Liu, R. Nazaryan, D. Pagliero, D. Suter, J. A. Reimer, A. Pines, and C. A. Meriles, Proceedings of the National Academy of Sciences **116**, 2512 (2019).
[32] W. S. Warren, Science **277**, 1688 (1997).
[33] S. L. Braunstein, C. M. Caves, R. Jozsa, N. Linden, S. Popescu, and R. Schack, Phys. Rev. Lett. **83**, 1054 (1999).
[34] R. Schack and C. M. Caves, Phys. Rev. A **60**, 4354 (1999).
[35] R. Jozsa and N. Linden, Proc. R. Soc. Lond. A **459**, 2011 (2003).
[36] E. Biham, G. Brassard, D. Kenigsberg, and T. Mor, Theoretical Computer Science **320**, 15 (2004).
[37] J. D. Bulnes, R. S. Sarthour, E. R. de Azevedo, F. A. Bonk, J. C. C. Freitas, A. P. Guimarães, T. J. Bonagamba, and I. S. Oliveira, "New considerations on the separability of very noisy mixed states and implications for NMR quantum computing," (2004), arXiv:quant-ph/0404020.
[38] B. P. Lanyon, M. Barbieri, M. P. Almeida, and A. G.

White, Phys. Rev. Lett. **101**, 200501 (2008).
[39] D. O. Soares-Pinto, R. Auccaise, J. Maziero, A. Gavini-Viana, R. M. Serra, and L. C. Céleri, Phil. Trans. R. Soc. A. **370**, 4821 (2012), arXiv:1202.1795 [quant-ph].
[40] R. Auccaise, J. Maziero, L. Céleri, D. Soares-Pinto, E. Deazevedo, R. Sarthour, I. Oliveira, and R. Serra, Physical Review Letters **107**, 070501 (2011).
[41] L. Viola, E. Knill, and S. Lloyd, Phys. Rev. Lett. **82**, 2417 (1999).
[42] L. Viola, S. Lloyd, and E. Knill, Phys. Rev. Lett. **83**, 4888 (1999).
[43] A. G. Kofman and G. Kurizki, Phys. Rev. Lett. **87**, 270405 (2001).
[44] A. G. Kofman and G. Kurizki, Phys. Rev. Lett. **93**, 130406 (2004).
[45] K. Khodjasteh and D. A. Lidar, Phys. Rev. Lett. **95**, 180501 (2005).
[46] G. S. Uhrig, Phys. Rev. Lett. **98**, 100504 (2007).
[47] A. M. Souza, G. A. Álvarez, and D. Suter, Phil. Trans. R. Soc. A **370**, 4748 (2012).
[48] G. A. Paz-Silva, A. T. Rezakhani, J. M. Dominy, and D. A. Lidar, Phys. Rev. Lett. **108**, 080501 (2012).
[49] D. Suter and G. A. Álvarez, Rev. Mod. Phys. **88**, 041001 (2016).
[50] G. Álvarez, D. Rao, L. Frydman, and G. Kurizki, Phys. Rev. Lett. **105**, 160401 (2010).
[51] G. A. Álvarez, M. Mishkovsky, E. P. Danieli, P. R. Levstein, H. M. Pastawski, and L. Frydman, Phys. Rev. A **81**, 060302 (R) (2010).
[52] A. Zwick, G. A. Álvarez, J. Stolze, and O. Osenda, "Robustness of spin-coupling distributions for perfect quantum state transfer", Phys. Rev. A **84**, 22311 (2011).
[53] C. O. Bretschneider, G. A. Álvarez, G. Kurizki, and L. Frydman, Phys. Rev. Lett. **108**, 140403 (2012).
[54] A. M. Souza, G. A. Álvarez, and D. Suter, Phys. Rev. A **86**, 050301(R) (2012).
[55] A. Ajoy and P. Cappellaro, Phys. Rev. Lett. **110**, 220503 (2013).
[56] A. Zwick, G. A. Álvarez, G. Bensky, and G. Kurizki, New J. Phys. **16**, 065021 (2014).
[57] T. D. Ladd, F. Jelezko, R. Laflamme, Y. Nakamura, C. Monroe, and J. L. O'Brien, Nature **464**, 45 (2010).
[58] R. Blatt and C. F. Roos, Nat. Phys. **8**, 277 (2012).
[59] G. A. Álvarez, R. Kaiser, and D. Suter, Ann. Phys. (Berlin) **525**, 833 (2013).
[60] I. Georgescu, S. Ashhab, and F. Nori, Rev. Mod. Phys. **86**, 153 (2014).
[61] I. H. Deutsch, PRX Quantum **1**, 020101 (2020).
[62] A. Mittermaier and L. Kay, Science **312**, 224 (2006).
[63] J. Bylander *et al.*, "Noise spectroscopy through dynamical decoupling with a superconducting flux qubit", Nat. Phys. **7**, 565 (2011).
[64] S. Steinert, F. Ziem, L. T. Hall, A. Zappe, M. Schweikert, N. Götz, A. Aird, G. Balasubramanian, L. Hollenberg, and J. Wrachtrup, Nat. Commun. **4**, 1607 (2013).
[65] H. J. Mamin *et al.*, Science **339**, 557 (2013).
[66] N. Shemesh, G. A. Álvarez, and L. Frydman, J. Magn. Reson. **237**, 49 (2013).
[67] L. T. Hall, D. A. Simpson, and L. C. L. Hollenberg, MRS Bulletin **38**, 162 (2013).
[68] A. Sushkov, I. Lovchinsky, N. Chisholm, R. Walsworth, H. Park, and M. Lukin, Phys. Rev. Lett. **113**, 197601 (2014).
[69] M. Loretz, S. Pezzagna, J. Meijer, and C. L. Degen, Appl. Phys. Lett. **104**, 033102 (2014).
[70] N. Shemesh, G. A. Álvarez, and L. Frydman, PLoS ONE **10**, e0133201 (2015).
[71] F. Casola, T. van der Sar, and A. Yacoby, Nat. Rev. Mater. **3**, 1 (2018).
[72] W. Rose, H. Haas, A. Q. Chen, N. Jeon, L. J. Lauhon, D. G. Cory, and R. Budakian, Phys. Rev. X **8**, 011030 (2018).
[73] V. Mukherjee, A. Zwick, A. Ghosh, X. Chen, and G. Kurizki, "Enhanced precision bound of low-temperature quantum thermometry via dynamical control", Communications Physics **2**, 1 (2019).
[74] H. Haas, S. Tabatabaei, W. Rose, P. Sahafi, M. Piscitelli, A. Jordan, P. Priyadarsi, N. Singh, B. Yager, P. J. Poole, D. Dalacu, and R. Budakian, Proceedings of the National Academy of Sciences **119**, e2209213119 (2022), publisher: Proceedings of the National Academy of Sciences.
[75] R. R. Ernst, G. Bodenhausen, and A. Wokaun, *Principles of Nuclear Magnetic Resonance in One and Two Dimensions* (Oxford University Press, USA, 1990).
[76] M. Levitt, John Wiley & Sons, Chichester UK (2008).
[77] P. T. Callaghan, *Translational Dynamics and Magnetic Resonance:Principles of Pulsed Gradient Spin Echo NMR* (Oxford University Press, 2011).
[78] M. A. Nielsen, E. Knill, and R. Laflamme, Nature **396**, 52 (1998).
[79] D. Cory, R. Laflamme, E. Knill, L. Viola, T. Havel, N. Boulant, G. Boutis, E. Fortunato, S. Lloyd, R. Martinez, C. Negrevergne, M. Pravia, Y. Sharf, G. Teklemariam, Y. Weinstein, and W. Zurek, Fortschr. Phys. **48**, 875 (2000).
[80] S. Sinha, J. Emerson, N. Boulant, E. M. Fortunato, T. F. Havel, and D. G. Cory, Quantum Information Processing **2**, 433 (2003).
[81] D. Lu, N. Xu, R. Xu, H. Chen, J. Gong, X. Peng, and J. Du, Phys. Rev. Lett. **107**, 020501 (2011).
[82] J. Li, R. Fan, H. Wang, B. Ye, B. Zeng, H. Zhai, X. Peng, and J. Du, Phys. Rev. X **7**, 031011 (2017).
[83] K. X. Wei, C. Ramanathan, and P. Cappellaro, Phys. Rev. Lett. **120**, 070501 (2018).
[84] K. X. Wei, P. Peng, O. Shtanko, I. Marvian, S. Lloyd, C. Ramanathan, and P. Cappellaro, Phys. Rev. Lett. **123**, 090605 (2019).
[85] C. M. Sánchez, A. K. Chattah, K. X. Wei, L. Buljubasich, P. Cappellaro, and H. M. Pastawski, Phys. Rev. Lett. **124**, 030601 (2020).
[86] F. D. Domínguez, M. C. Rodríguez, R. Kaiser, D. Suter, and G. A. Álvarez, Phys. Rev. A **104**, 012402 (2021).
[87] G. Kucsko *et al.*, "Nanometre-scale thermometry in a living cell", Nature **500**, 54 (2013).
[88] P. Neumann *et al.*, "High-precision nanoscale temperature sensing using single defects in diamond", Nano lett. **13**, 2738 (2013).
[89] C. Uhlig, R. S. Sarthour, I. S. Oliveira, and A. Souza, Quantum Information Processing **18**, 1 (2019).
[90] J. Maze, P. Stanwix, J. Hodges, S. Hong, J. Taylor, P. Cappellaro, L. Jiang, M. G. Dutt, E. Togan, A. Zibrov, *et al.*, "Nanoscale magnetic sensing with an individual electronic spin in diamond", Nature **455**, 644 (2008).
[91] G. Balasubramanian *et al.*, "Nanoscale imaging magnetometry with diamond spins under ambient conditions", Nature **455**, 648 (2008).

[92] G. A. Álvarez, N. Shemesh, and L. Frydman, Sci Rep **7**, 3311 (2017).

[93] A. Zwick, D. Suter, G. Kurizki, and G. A. Álvarez, Phys. Rev. Applied **14**, 024088 (2020).

[94] M. Capiglioni, A. Zwick, P. Jiménez, and G. A. Álvarez, Phys. Rev. Applied **15**, 014045 (2021).

[95] D. Le Sage *et al.*, "Optical magnetic imaging of living cells", Nature **496**, 486 (2013).

[96] M. S. Grinolds *et al.*, "Subnanometre resolution in three-dimensional magnetic resonance imaging of individual dark spins", Nat. Nanotechnol. **9**, 279 (2014).

[97] A. Ajoy, U. Bissbort, M. D. Lukin, R. L. Walsworth, and P. Cappellaro, Phys. Rev. X **5**, 011001 (2015).

[98] C. L. Degen, F. Reinhard, and P. Cappellaro, Rev. Mod. Phys. **89**, 035002 (2017).

[99] J. A. Jones, S. D. Karlen, J. Fitzsimons, A. Ardavan, S. C. Benjamin, G. A. D. Briggs, and J. J. L. Morton, Science **324**, 1166 (2009).

[100] S. Zhou, M. Zhang, J. Preskill, and L. Jiang, Nat Commun **9**, 78 (2018).

[101] L. T. Hall, G. C. G. Beart, E. A. Thomas, D. A. Simpson, L. P. McGuinness, J. H. Cole, J. H. Manton, R. E. Scholten, F. Jelezko, J. Wrachtrup, S. Petrou, and L. C. L. Hollenberg, Sci Rep **2**, 401 (2012).

[102] A. Ermakova *et al.*, "Detection of a few metallo-protein molecules using color centers in nanodiamonds", Nano lett. **13**, 3305 (2013).

[103] M. Kost, J. Cai, and M. B. Plenio, "Resolving single molecule structures with nitrogen-vacancy centers in diamond", Sci. Rep. **5**, 11007 (2015).

[104] F. Shi, Q. Zhang, P. Wang, H. Sun, J. Wang, X. Rong, M. Chen, C. Ju, F. Reinhard, H. Chen, J. Wrachtrup, J. Wang, and J. Du, Science **347**, 1135 (2015).

[105] I. Lovchinsky, A. O. Sushkov, E. Urbach, N. P. de Leon, S. Choi, K. De Greve, R. Evans, R. Gertner, E. Bersin, C. Muller, L. McGuinness, F. Jelezko, R. L. Walsworth, H. Park, and M. D. Lukin, Science **351**, 836 (2016).

[106] E. Knill, I. Chuang, and R. Laflamme, Phys. Rev. A **57**, 3348 (1998).

[107] D. M. Patterson, A. R. Padhani, and D. J. Collins, Nat. Rev. Clin. Oncol. **5**, 220 (2008).

[108] A. R. Padhani, G. Liu, D. M. Koh, T. L. Chenevert, H. C. Thoeny, T. Takahara, A. Dzik-Jurasz, B. D. Ross, M. Van Cauteren, D. Collins, D. A. Hammoud, G. J. S. Rustin, B. Taouli, and P. L. Choyke, Neoplasia **11**, 102 (2009).

[109] V. Drago, C. Babiloni, D. Bartrés-Faz, A. Caroli, B. Bosch, T. Hensch, M. Didic, H.-W. Klafki, M. Pievani, J. Jovicich, *et al.*, Journal of Alzheimer's Disease **26**, 159 (2011).

[110] N. S. White, T. B. Leergaard, H. D'Arceuil, J. G. Bjaalie, and A. M. Dale, Hum. Brain Mapp. **34**, 327 (2013).

[111] N. S. White, C. R. McDonald, N. Farid, J. Kuperman, D. Karow, N. M. Schenker-Ahmed, H. Bartsch, R. Rakow-Penner, D. Holland, A. Shabaik, A. Bjørnerud, T. Hope, J. Hattangadi-Gluth, M. Liss, J. K. Parsons, C. C. Chen, S. Raman, D. Margolis, R. E. Reiter, L. Marks, S. Kesari, A. J. Mundt, C. J. Kaine, B. S. Carter, W. G. Bradley, and A. M. Dale, Cancer Res. **74**, 4638 (2014).

[112] C. Enzinger, F. Barkhof, O. Ciccarelli, M. Filippi, L. Kappos, M. A. Rocca, S. Ropele, À. Rovira, T. Schneider, N. de Stefano, H. Vrenken, C. Wheeler-Kingshott, J. Wuerfel, F. Fazekas, and o. and, Nat. Rev. Neurol. **11**, 676 (2015).

[113] A. Wacker, J. E. Weigand, S. R. Akabayov, N. Altincekic, J. K. Bains, E. Banijamali, O. Binas, J. Castillo-Martinez, E. Cetiner, B. Ceylan, L.-Y. Chiu, J. Davila-Calderon, K. Dhamotharan, E. Duchardt-Ferner, J. Ferner, L. Frydman, B. Fürtig, J. Gallego, J. T. Grün, C. Hacker, C. Haddad, M. Hähnke, M. Hengesbach, F. Hiller, K. F. Hohmann, D. Hymon, V. de Jesus, H. Jonker, H. Keller, B. Knezic, T. Landgraf, F. Löhr, L. Luo, K. R. Mertinkus, C. Muhs, M. Novakovic, A. Oxenfarth, M. Palomino-Schätzlein, K. Petzold, S. A. Peter, D. J. Pyper, N. S. Qureshi, M. Riad, C. Richter, K. Saxena, T. Schamber, T. Scherf, J. Schlagnitweit, A. Schlundt, R. Schnieders, H. Schwalbe, A. Simba-Lahuasi, S. Sreeramulu, E. Stirnal, A. Sudakov, J.-N. Tants, B. S. Tolbert, J. Vögele, L. Weiss, J. Wirmer-Bartoschek, M. A. Wirtz Martin, J. Wöhnert, and H. Zetzsche, Nucleic Acids Research **48**, 12415 (2020).

[114] P. Basser, J. Mattiello, and D. LeBihan, Biophys. J. **66**, 259 (1994).

[115] D. Le Bihan, Nat. Rev. Neurosci. **4**, 469 (2003).

[116] Y. Assaf, T. Blumenfeld-Katzir, Y. Yovel, and P. J. Basser, Magnetic Resonance in Medicine: An Official Journal of the International Society for Magnetic Resonance in Medicine **59**, 1347 (2008).

[117] D. C. Alexander, P. L. Hubbard, M. G. Hall, E. A. Moore, M. Ptito, G. J. Parker, and T. B. Dyrby, Neuroimage **52**, 1374 (2010).

[118] H. H. Ong and F. W. Wehrli, Neuroimage **51**, 1360 (2010).

[119] J. C. Gore, J. Xu, D. C. Colvin, T. E. Yankeelov, E. C. Parsons, and M. D. Does, NMR Biomed. **23**, 745 (2010).

[120] M. E. Komlosh, E. Ozarslan, M. J. Lizak, F. Horkay, V. Schram, N. Shemesh, Y. Cohen, and P. J. Basser, J. Magn. Reson. **208**, 128 (2011).

[121] J. Xu, H. Li, K. D. Harkins, X. Jiang, J. Xie, H. Kang, M. D. Does, and J. C. Gore, Neuroimage **103**, 10 (2014).

[122] N. Shemesh, J. T. Rosenberg, J.-N. Dumez, S. C. Grant, and L. Frydman, PLOS ONE **12**, e0185232 (2017), publisher: Public Library of Science.

[123] D. C. Alexander, T. B. Dyrby, M. Nilsson, and H. Zhang, NMR in Biomedicine **32**, e3841 (2019).

[124] J. Xu, X. Jiang, H. Li, L. R. Arlinghaus, E. T. McKinley, S. P. Devan, B. M. Hardy, J. Xie, H. Kang, A. B. Chakravarthy, and J. C. Gore, arXiv e-prints , arXiv:1905.07818 (2019), arXiv:1905.07818 [physics.bio-ph].

[125] M. Yon, J. P. de Almeida Martins, Q. Bao, M. D. Budde, L. Frydman, and D. Topgaard, NMR in Biomedicine **33**, e4355 (2020), _eprint: https://onlinelibrary.wiley.com/doi/pdf/10.1002/nbm.4355.

[126] W. Zurek, Rev. Mod. Phys. **75**, 715 (2003).

[127] H. M. Pastawski, P. R. Levstein, G. Usaj, J. Raya, and J. A. Hirschinger, Physica A **283**, 166 (2000).

[128] R. A. Jalabert and H. M. Pastawski, Phys. Rev. Lett. **86**, 2490 (2001).

[129] P. Jacquod and C. Petitjean, Adv. Phys. **58**, 67 (2009).

[130] A. Goussev, R. A. Jalabert, H. M. Pastawski, and D. A. Wisniacki, Scholarpedia **7**, 11687 (2012).

[131] S. Popescu, A. J. Short, and A. Winter, Nat. Phys. **2**,

754 (2006).
[132] M. Rigol, V. Dunjko, and M. Olshanii, Nature **452**, 854 (2008).
[133] G. A. Álvarez, E. P. Danieli, P. R. Levstein, and H. M. Pastawski, Phys. Rev. Lett. **101**, 120503 (2008).
[134] R. Nandkishore and D. A. Huse, Annu. Rev. Condens. Matter Phys. **6**, 15 (2015).
[135] D. A. Abanin, E. Altman, I. Bloch, and M. Serbyn, Rev. Mod. Phys. **91**, 021001 (2019).
[136] R. J. Lewis-Swan, A. Safavi-Naini, A. M. Kaufman, and A. M. Rey, Nat. Rev. Phys. **1**, 627 (2019).
[137] A. Zwick, G. A. Álvarez, and G. Kurizki, Phys. Rev. Applied **5**, 014007 (2016).
[138] M. Gal, P. Schanda, B. Brutscher, and L. Frydman, J. Am. Chem. Soc. **129**, 1372 (2007).
[139] A. Corazza, E. Rennella, P. Schanda, M. C. Mimmi, T. Cutuil, S. Raimondi, S. Giorgetti, F. Fogolari, P. Viglino, L. Frydman, M. Gal, V. Bellotti, B. Brutscher, and G. Esposito, J. Biol. Chem. **285**, 5827 (2010).
[140] M. Novakovic, G. L. Olsen, G. Pintér, D. Hymon, B. Fürtig, H. Schwalbe, and L. Frydman, Proceedings of the National Academy of Sciences **117**, 2449 (2020), publisher: Proceedings of the National Academy of Sciences.
[141] P. W. Schaefer, P. E. Grant, and R. G. Gonzalez, Radiology **217**, 331 (2000).
[142] D. Le Bihan, S.-i. Urayama, T. Aso, T. Hanakawa, and H. Fukuyama, Proc. Nat. Acad. Sci. **103**, 8263 (2006).
[143] E. R. Jenista, A. M. Stokes, R. T. Branca, and W. S. Warren, J. Chem. Phys. **131**, 204510 (2009).
[144] A. Tal and L. Frydman, Prog. Nucl. Magn. Reson. Spectrosc. **57**, 241 (2010).
[145] E. Hahn, Phys. Rev. **80**, 580 (1950).
[146] H. Carr and E. Purcell, Phys. Rev. **94**, 630 (1954).
[147] S. Meiboom and D. Gill, Rev. Sci. Instrum. **29**, 688 (1958).
[148] U. Haeberlen and J. S. Waugh, Phys. Rev. **175**, 453 (1968).
[149] G. Kurizki and A. Zwick, in *"From Coherent to Incoherent Dynamical Control of Open Quantum Systems", Advances in Chemical Physics* (Wiley-Blackwell, 2016) Chap. 4, pp. 137–218.
[150] A. G. Kofman and G. Kurizki, Phys. Rev. A **54**, R3750 (1996).
[151] A. G. Kofman and G. Kurizki, Nature **405**, 546 (2000).
[152] L. Xiao and J. A. Jones, Physics Letters A **359**, 424 (2006).
[153] N. Erez, G. Gordon, M. Nest, and G. Kurizki, Nature **452**, 724 (2008).
[154] G. Kurizki and A. Zwick, in *"From coherent to incoherent dynamical control of open quantum systems", To appear in Adv. Chem. Phys. 159*, edited by P. Brumer, S. A. Rice, and A. R. Dinner (John Wiley, 2015).
[155] M. J. Biercuk, H. Uys, A. P. VanDevender, N. Shiga, W. M. Itano, and J. J. Bollinger, Nature **458**, 996 (2009).
[156] J. Du, X. Rong, N. Zhao, Y. Wang, J. Yang, and R. B. Liu, Nature **461**, 1265 (2009).
[157] G. de Lange, *et al.*, Science **330**, 60 (2010).
[158] C. A. Ryan, J. S. Hodges, and D. G. Cory, Phys. Rev. Lett. **105**, 200402 (2010).
[159] A. Ajoy, G. A. Álvarez, and D. Suter, Phys. Rev. A **83**, 032303 (2011).
[160] P. T. Callaghan, *Principles of Nuclear Magnetic Resonance Microscopy* (Oxford University Press, 1993).
[161] Ł. Cywiński, R. M. Lutchyn, C. P. Nave, and S. Das Sarma, Phys. Rev. B **77**, 174509 (2008).
[162] B. Misra and E. C. G. Sudarshan, J. Math. Phys. **18**, 756 (1977).
[163] R. Tycko, Phys. Rev. Lett. **99**, 187601 (2007).
[164] P. Facchi, D. A. Lidar, and S. Pascazio, Phys. Rev. A **69**, 0302314 (2004).
[165] C. A. Meriles, L. Jiang, G. Goldstein, J. S. Hodges, J. Maze, M. D. Lukin, and P. Cappellaro, J. Chem. Phys. **133**, 124105 (2010).
[166] M. Kuffer, A. Zwick, and G. A. Álvarez, PRX Quantum **3**, 020321 (2022).
[167] G. Gordon and G. Kurizki, New J. Phys. **10**, 045005 (2008).
[168] J. Clausen, G. Bensky, and G. Kurizki, Phys. Rev. Lett. **104**, 040401 (2010).
[169] S. Kotler, N. Akerman, Y. Glickman, and R. Ozeri, Phys. Rev. Lett. **110**, 110503 (2013).
[170] Y. Sung, F. Beaudoin, L. M. Norris, F. Yan, D. K. Kim, J. Y. Qiu, U. von Lüpke, J. L. Yoder, T. P. Orlando, S. Gustavsson, L. Viola, and W. D. Oliver, Nat. Commun. **10**, 3715 (2019).
[171] Y. Sung, A. Vepsäläinen, J. Braumüller, F. Yan, J. I.-J. Wang, M. Kjaergaard, R. Winik, P. Krantz, A. Bengtsson, A. J. Melville, B. M. Niedzielski, M. E. Schwartz, D. K. Kim, J. L. Yoder, T. P. Orlando, S. Gustavsson, and W. D. Oliver, Nat. Commun. **12**, 967 (2021).
[172] W.-L. Ma, G. Wolfowicz, N. Zhao, S.-S. Li, J. J. L. Morton, and R.-B. Liu, Nat. Commun. **5**, 4822 (2014).
[173] G. Kurizki, E. Shahmoon, and A. Zwick, Phys. Scr. **90**, 128002 (2015).
[174] D. F. Wise, J. J. L. Morton, and S. Dhomkar, PRX Quantum **2**, 010316 (2021).
[175] H.-P. Breuer, F. Petruccione, *et al.*, *The theory of open quantum systems* (Oxford University Press on Demand, 2002).
[176] A. Abragam, *Principles of Nuclear Magnetism*, International Series of Monographs on Physics (Oxford University Press, Oxford, New York, 1983).
[177] G. Gordon, N. Erez, and G. Kurizki, J. Phys. B: At. Mol. Opt. Phys. **40**, S75 (2007), publisher: IOP Publishing.
[178] G. A. Paz-Silva and L. Viola, Phys. Rev. Lett. **113**, 250501 (2014).
[179] L. M. Norris, G. A. Paz-Silva, and L. Viola, Phys. Rev. Lett. **116**, 150503 (2016).
[180] J. R. Klauder and P. W. Anderson, Phys. Rev. **125**, 912 (1962).
[181] J. M. Taylor, P. Cappellaro, L. Childress, L. Jiang, D. Budker, P. R. Hemmer, A. Yacoby, R. Walsworth, and M. D. Lukin, Nat. Phys. **4**, 810 (2008).
[182] F. Dolde, H. Fedder, M. W. Doherty, T. Nöbauer, F. Rempp, G. Balasubramanian, T. Wolf, F. Reinhard, L. C. L. Hollenberg, F. Jelezko, and J. Wrachtrup, Nature Physics **7**, 459 (2011).
[183] L. P. McGuinness, L. T. Hall, A. Stacey, D. A. Simpson, C. D. Hill, J. H. Cole, K. Ganesan, B. C. Gibson, S. Prawer, P. Mulvaney, F. Jelezko, J. Wrachtrup, R. E. Scholten, and L. C. L. Hollenberg, "Ambient nanoscale sensing with single spins using quantum decoherence", New J. Phys. **15**, 073042 (2013).
[184] D. Suter and F. Jelezko, Progress in Nuclear Magnetic

Resonance Spectroscopy **98-99**, 50 (2017).
[185] G. Gordon, G. Kurizki, and D. A. Lidar, Phys. Rev. Lett. **101**, 010403 (2008).
[186] J. Clausen, G. Bensky, and G. Kurizki, Phys. Rev. A **85**, 052105 (2012).
[187] T. Chalermpusitarak, B. Tonekaboni, Y. Wang, L. M. Norris, L. Viola, and G. A. Paz-Silva, PRX Quantum **2**, 030315 (2021).
[188] I. Almog, Y. Sagi, G. Gordon, G. Bensky, G. Kurizki, and N. Davidson, J. Phys. B: At. Mol. Opt. Phys. **44**, 154006 (2011).
[189] F. Yan, S. Gustavsson, J. Bylander, X. Jin, F. Yoshihara, D. G. Cory, Y. Nakamura, T. P. Orlando, and W. D. Oliver, Nat. Commun. **4**, 2337 (2013).
[190] R. Kimmich, *NMR: Tomography, Diffusometry, Relaxometry* (Springer, 1997).
[191] R. Kimmich and E. Anoardo, ChemInform **35** (2004), 10.1002/chin.200447278, _eprint: https://onlinelibrary.wiley.com/doi/pdf/10.1002/chin.200447278.
[192] G. Gordon and G. Kurizki, Phys. Rev. A **83**, 032321 (2011).
[193] C. Barthel, J. Medford, C. M. Marcus, M. P. Hanson, and A. C. Gossard, Phys. Rev. Lett. **105**, 266808 (2010).
[194] S. Pasini and G. S. Uhrig, Phys. Rev. A **81**, 012309 (2010).
[195] J. Medford, Ł. Cywiński, C. Barthel, C. M. Marcus, M. P. Hanson, and A. C. Gossard, Phys. Rev. Lett. **108**, 086802 (2012).
[196] G. A. Álvarez, N. Shemesh, and L. Frydman, J. Chem. Phys. **140**, 084205 (2014).
[197] S. Braunstein and C. Caves, Physical Review Letters **72**, 3439 (1994).
[198] M. G. A. Paris, "Quantum estimation for quantum technology", Int. J. Quantum Inf. **07**, 12 (2009).
[199] A. Zwick, G. A. Álvarez, and G. Kurizki, Phys. Rev. A **94**, 042122 (2016).
[200] C. Benedetti and M. G. A. Paris, Phys. Lett. A **378**, 2495 (2014).
[201] A. T. Watson and C. T. P. Chang, Progress in Nuclear Magnetic Resonance Spectroscopy **31**, 343 (1997).
[202] M. Fleury and F. Deflandre, Magnetic Resonance Imaging **21**, 385 (2003).
[203] Y. Song, H. Cho, T. Hopper, A. Pomerantz, and P. Sun, Journal of Chemical Physics **128**, 052212 (2008).
[204] P. T. Callaghan, C. H. Arns, P. Galvosas, M. W. Hunter, Y. Qiao, and K. E. Washburn, Magnetic Resonance Imaging **25**, 441 (2007).
[205] M. N. dÉurydice, E. T. Montrazi, C. A. Fortulan, and T. J. Bonagamba, J. Chem. Phys. **144**, 204201 (2016).
[206] K. J. Packer, J. Magn. Reson. **9**, 438 (1973).
[207] Y.-Q. Song, S. Ryu, and P. N. Sen, Nature **406**, 178 (2000).
[208] Y.-Q. Song, Concepts Magn. Reson. **18A**, 97 (2003).
[209] S. Han, Y. Song, F. Cho, S. Ryu, G. Cho, Y. Song, and H. Cho, J. Magn. Reson. **212**, 386 (2011).
[210] H. Cho, E. Sigmund, and Y. Song, Materials **5**, 590 (2012).
[211] G. Di Pietro, M. Palombo, and S. Capuani, Appl Magn Reson **45**, 771 (2014).
[212] Y. Zhang, L. Xiao, G. Liao, and B. Blümich, Journal of Magnetic Resonance **267**, 37 (2016).
[213] J. E. Fajardo and G. A. Álvarez, in *Proc. Intl. Soc. Mag. Reson. Med.*, Vol. 29 (2021) p. 1716.
[214] P. T. Callaghan, A. Coy, D. MacGowan, K. J. Packer, and F. O. Zelaya, Nature **351**, 467 (1991).
[215] P. T. Callaghan, A. Coy, T. Halpin, D. MacGowan, K. J. Packer, and F. O. Zelaya, The Journal of chemical physics **97**, 651 (1992).
[216] J. Stepišnik, Physica B **183**, 343 (1993).
[217] P. T. Callaghan, J. Magn. Reson. **129**, 74 (1997).
[218] S. Lasic, J. Stepisnik, and A. Mohoric, J. Magn. Reson. **182**, 208 (2006).
[219] J. Stepisnik, S. Lasic, A. Mohorix, I. Sersa, and A. Sepe, J. Magn. Reson. **182**, 195 (2006).
[220] J. Veraart, D. Nunes, U. Rudrapatna, E. Fieremans, D. K. Jones, D. S. Novikov, and N. Shemesh, eLife **9**, e49855 (2020).
[221] P. T. Callaghan and J. Stepisnik, J. Magn. Reson. **117**, 118 (1995).
[222] P. Z. Sun, J. G. Seland, and D. Cory, Journal of Magnetic Resonance **161**, 168 (2003).
[223] G. Zheng and W. S. Price, Concepts in Magnetic Resonance Part A **30A**, 261 (2007).
[224] D. S. Grebenkov, Rev. Mod. Phys. **79**, 1077 (2007).
[225] J. Stepišnik, Physica B **270**, 110 (1999).
[226] I. Drobnjak, H. Zhang, A. Ianuş, E. Kaden, and D. C. Alexander, Magnetic resonance in medicine **75**, 688 (2016).
[227] M. Nilsson, S. Lasic, I. Drobnjak, D. Topgaard, and C.-F. Westin, NMR Biomed. **30**, e3711 (2017), e3711 nbm.3711, https://onlinelibrary.wiley.com/doi/pdf/10.1002/nbm.3711.
[228] D. S. Novikov, E. Fieremans, S. N. Jespersen, and V. G. Kiselev, NMR in Biomedicine **32**, e3998 (2019).
[229] R. C. Wayne and R. M. Cotts, Phys. Rev. **151**, 264 (1966), publisher: American Physical Society.
[230] B. Robertson, Phys. Rev. **151**, 273 (1966), publisher: American Physical Society.
[231] E. O. Stejskal and J. E. Tanner, J. Chem. Phys. **42**, 288 (1965).
[232] J. E. Tanner, The Journal of Chemical Physics **52**, 2523 (1970).
[233] A. Shukla, M. Sharma, and T. Mahesh, Chemical Physics Letters **592**, 227 (2014).
[234] M. Giménez, P. Jiménez, L. Pedraza Pérez, D. Betancourth, A. Zwick, and G. A. Álvarez, Proc. Intl. Soc. Mag. Reson. Med. **29**, 3418 (2021).
[235] M. Capiglioni, A. Zwick, P. Jiménez, and G. A. Álvarez, Proc. Intl. Soc. Mag. Reson. Med. **29**, 2036 (2021).
[236] W.-K. Rhim, A. Pines, and J. S. Waugh, Phys. Rev. B **3**, 684 (1971).
[237] S. Zhang, B. H. Meier, and R. R. Ernst, Phys. Rev. Lett. **69**, 2149 (1992), copyright (C) 2009 The American Physical Society; Please report any problems to prola@aps.org.
[238] D. Suter and R. R. Ernst, Phys. Rev. B **32**, 5608 (1985).
[239] W. Zhang and D. G. Cory, Phys. Rev. Lett. **80**, 1324 (1998).
[240] J. Baum, M. Munowitz, A. N. Garroway, and A. Pines, J. Chem. Phys. **83**, 2015 (1985).
[241] M. Munowitz and A. Pines, in *Advances in Chemical Physics*, Vol. 66 (John Wiley & Sons, Inc., Hoboken, NJ, USA, 1986) pp. 1–152.
[242] J. Baum, K. K. Gleason, A. Pines, A. N. Garroway, and J. A. Reimer, Phys. Rev. Lett. **56**, 1377 (1986).
[243] M. Munowitz, A. Pines, and M. Mehring, J. Chem. Phys. **86**, 3172 (1987).
[244] S. Lacelle, Adv. Magn. Opt. Res. **16**, 173 (1991).

[245] H. G. Krojanski and D. Suter, Phys. Rev. Lett. **93**, 090501 (2004).
[246] C. E. Hughes, Prog. Nucl. Magn. Reson. Spectrosc. **45**, 301 (2004).
[247] C. M. Sánchez, P. R. Levstein, L. Buljubasich, H. M. Pastawski, and A. K. Chattah, Phil. Trans. R. Soc. A. **374**, 20150155 (2016).
[248] M. Gärttner, J. G. Bohnet, A. Safavi-Naini, M. L. Wall, J. J. Bollinger, and A. M. Rey, Nat. Phys. **13**, 781 (2017).
[249] M. Gärttner, P. Hauke, and A. M. Rey, Phys. Rev. Lett. **120**, 040402 (2018).
[250] M. Niknam, L. F. Santos, and D. G. Cory, Phys. Rev. Research **2**, 013200 (2020).
[251] Y. Sekino and L. Susskind, J. High Energy Phys. **2008**, 065 (2008).
[252] N. Lashkari, D. Stanford, M. Hastings, T. Osborne, and P. Hayden, J. High Energy Phys. **2013**, 22 (2013).
[253] B. Swingle, Nat. Phys. **14**, 988 (2018).
[254] F. D. Domínguez and G. A. Álvarez, Physical Review A **104**, 062406 (2021).
[255] J. Maldacena, S. H. Shenker, and D. Stanford, J. High Energy Phys. **2016**, 106 (2016).
[256] C. M. Sánchez, A. K. Chattah, and H. M. Pastawski, Phys. Rev. A **105**, 052232 (2022).
[257] B. Yan, L. Cincio, and W. H. Zurek, Phys. Rev. Lett. **124**, 160603 (2020).
[258] G. A. Álvarez and D. Suter, Phys. Rev. A **84**, 012320 (2011).
[259] C. P. Slichter, *Principles of magnetic resonance* (Springer, 1996).
[260] T. Gorin, T. Prosen, T. H. Seligman, and M. Žnidarič, Physics Reports **435**, 33 (2006).
[261] P. Hosur, X.-L. Qi, D. A. Roberts, and B. Yoshida, J. High Energy Phys. **2016**, 4 (2016).
[262] A. K. Khitrin, Chem. Phys. Lett. **274**, 217 (1997).
[263] H. G. Krojanski and D. Suter, Phys. Rev. Lett. **97**, 150503 (2006).
[264] D. Levy and K. Gleason, J. Phys. Chem. **96**, 8125 (1992).
[265] S. Lacelle, S. J. Hwang, and B. C. Gerstein, J. Chem. Phys. **99**, 8407 (1993).
[266] C. M. Sánchez, R. H. Acosta, P. R. Levstein, H. M. Pastawski, and A. K. Chattah, Phys. Rev. A **90**, 042122 (2014).
[267] O. W. Sørensen, M. H. Levitt, and R. R. Ernst, J. Magn. Reson. **55**, 104 (1983).
[268] C. Griesinger, O. W. Sørensen, and R. R. Ernst, J. Chem. Phys. **85**, 6837 (1986).
[269] J. Dalibard, Y. Castin, and K. Mölmer, Phys. Rev. Lett. **68**, 580 (1992).
[270] G. Teklemariam, E. M. Fortunato, C. C. López, J. Emerson, J. P. Paz, T. F. Havel, and D. G. Cory, Phys. Rev. A **67**, 062316 (2003).
[271] L. Braunschweiler and R. Ernst, Journal of Magnetic Resonance (1969) **53**, 521 (1983).
[272] P. Caravatti, L. Braunschweiler, and R. Ernst, Chemical physics letters **100**, 305 (1983).
[273] B. Luy, O. Schedletzky, and S. J. Glaser, Journal of Magnetic Resonance **138**, 19 (1999).
[274] E. Ferraro, M. Scala, R. Migliore, and A. Napoli, Physica Scripta **T140**, 014042 (2010).
[275] A. Sergeevich, A. Chandran, J. Combes, S. D. Bartlett, and H. M. Wiseman, Phys. Rev. A **84**, 052315 (2011).
[276] C. E. Granade, C. Ferrie, N. Wiebe, and D. G. Cory, New J. Phys. **14**, 103013 (2012).
[277] P. Cappellaro, Phys. Rev. A **85**, 030301 (2012).
[278] N. Bar-Gill, L. M. Pham, C. Belthangady, D. Le Sage, P. Cappellaro, J. R. Maze, M. D. Lukin, A. Yacoby, and R. Walsworth, Nat. Commun. **3**, 858 (2012).
[279] N. B. Manson, J. P. Harrison, and M. J. Sellars, Phys. Rev. B **74**, 104303 (2006).

- Quantum control and estimation tools probe physical, chemical, biological processes
- Efficient quantum sensing for maximizing relevant environmental information
- Biological tissue microstructure characterization with diffusion weighting imaging
- Assessing fragility of quantum information dynamics in out-of-equilibrium systems
- Selective estimation of spin-spin couplings and online learning control designs

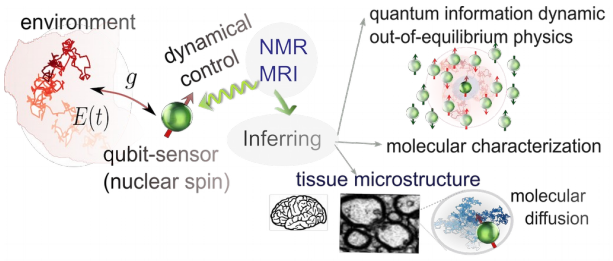
environment
dynamical control
NMR
MRI
g
$E(t)$
qubit-sensor
(nuclear spin)
Inferring
quantum information dynamic
out-of-equilibrium physics
molecular characterization
tissue microstructure
molecular
diffusion

Declaration of interests

☒ The authors declare that they have no known competing financial interests or personal relationships that could have appeared to influence the work reported in this paper.

☐The authors declare the following financial interests/personal relationships which may be considered as potential competing interests: